

Open Source Algorithm for Detecting Sea Ice Surface Features in High Resolution Optical Imagery

Nicholas C. Wright¹, Christopher M. Polashenski^{1,2}

¹Thayer School of Engineering, Dartmouth College, Hanover, NH, USA

²U.S. Army Cold Regions Research and Engineering Laboratories, Hanover, NH, USA

Correspondence to: N. C. Wright (ncwright.th@dartmouth.edu)

Abstract. Snow, ice, and melt ponds cover the surface of the Arctic Ocean in fractions that change throughout the seasons. These surfaces control albedo and exert tremendous influence over the energy balance in the Arctic. Increasingly available m- to dm-scale resolution optical imagery captures the evolution of the ice and ocean surface state visually, but methods for quantifying coverage of key surface types from raw imagery are not yet well established. Here we present an open source system designed to provide a standardized, automated, and reproducible technique for processing optical imagery of sea ice. The method classifies surface coverage into three main categories: Snow and bare ice, melt ponds and submerged ice, and open water. The method is demonstrated on imagery from four sensor platforms and on imagery spanning from spring thaw to fall freeze-up. Tests show the classification accuracy of this method typically exceeds 96%. To facilitate scientific use, we evaluate the minimum observation area required for reporting a representative sample of surface coverage. We provide an open source distribution of this algorithm and associated training data sets and suggest the community consider this a step towards standardizing optical sea ice imagery processing. We hope to encourage future collaborative efforts to improve the code base and to analyze large datasets of optical sea ice imagery.

1 Introduction

The surface of the sea ice-ocean system exhibits many different forms. Snow, ice, ocean, and melt ponds cover the surface in fractions that change throughout the seasons. The relative fractions of these surfaces covering the Arctic ocean are undergoing substantial change due to rapid loss of sea ice (Stroeve et al., 2012), increase in the duration of melt (Markus et al., 2009; Stroeve et al., 2014), decrease in sea ice age (Maslanik et al., 2011), and decrease in sea ice thickness (Kwok and Rothrock, 2009; Laxon et al., 2013) over recent decades. As a whole, the changes are reducing albedo and enhancing the absorption of solar radiation, triggering an ice albedo feedback (Curry et al., 1995; Perovich et al., 2008; Pistone et al., 2014). Large-scale remote sensing has been instrumental in documenting the ongoing change in ice extent (Parkinson and Comiso, 2013), thickness (Kurtz et al., 2013; Kwok and Rothrock, 2009; Laxon et al., 2013), and surface melt state (Markus et al., 2009). An increasing focus on improving prediction of future sea ice and climate states, however, has also created substantial interest in better observing, characterizing, and modeling the *processes* that drive changes in albedo-relevant sea ice surface conditions such as melt pond formation, which occur at smaller length scales. For these, observations that resolve surface conditions explicitly are needed to understand the underlying causes of the seasonal and spatial evolution of albedo in a more sophisticated way.

34 Explicitly sensing the key aspects of the sea ice surface, including melt pond coverage, degree of deformation, floe
35 size, and lead distributions, requires evaluating the surface at meter to decimeter scale resolution. Variability in the
36 spatial coverage and morphology of these surface characteristics, however, occurs over hundreds of meters to tens of
37 kilometers. Estimates of aggregate scale surface coverage fraction must therefore be made at high resolution over
38 sample domains of many square kilometers. Quantifying the relative abundance of surface types over domains of
39 multi-kilometer scale from manned ground campaigns is both time consuming and impractical. Remote sensing
40 provides a more viable approach for studying these multi-kilometer areas. High resolution optical imagery (e.g. Figure
41 1) visually captures the surface features of interest, but the methods for analyzing this imagery remain under-
42 developed.

43 The need for remote sensing methods enabling quantification of meter-scale sea ice surface characteristics has
44 been well recognized, and efforts have been made to address it. Recent developments in remote sensing of sea ice
45 surface conditions fall into two categories: (1) methods using low-medium resolution satellite imagery (i.e. having
46 pixel sizes larger than the typical ice surface feature size) with spectral un-mixing type algorithms to derive aggregate
47 measures of sub-pixel phenomena (e.g. for melt ponds Markus et al., 2003; Rösel et al., 2012; Rösel and Kaleschke,
48 2011; Tschudi et al., 2008) and (2) methods using higher resolution satellite or airborne imagery (i.e. having pixel size
49 smaller than the typical scale of ice surface features) that is capable of explicitly resolving features (e.g. [Arntsen et
50 al., 2015](#); [Fetterer and Untersteiner, 1998](#); [Inoue et al., 2008](#); [Kwok, 2014](#); [Lu et al., 2010](#); [Miao et al., 2015](#); [Perovich
51 et al., 2002b](#); [Renner et al., 2014](#); [Webster et al., 2015](#)). The first category, those derived from low-medium resolution
52 imagery, have notable strengths in their frequent sampling and basin-wide coverage. They cannot, however, provide
53 detailed statistics on the morphology of surface features necessary for assessing our process-based understanding and
54 have substantial uncertainty due to ambiguity in spectral signal un-mixing. The second category – observations at high
55 resolutions which explicitly resolve surface properties – can provide these detailed statistics, but were historically
56 limited by a dearth of data acquisitions. Recent increases in imagery availability from formerly classified defense
57 (Kwok, 2014) or commercial satellites (e.g. DigitalGlobe), and increases in manned flights over the Arctic (e.g.
58 IceBridge, SIZRS) have substantially reduced this constraint for optical imagery. Likely increases in collection of
59 imagery from UAV's (DeMott and Hill, 2016) and increases in satellite imaging bandwidth (e.g. DigitalGlobe
60 WorldView 4 launched in 2016) suggest that availability of high resolution imagery will continue to increase.

61 Processing high resolution sea ice imagery to derive useful metrics quantifying surface state, however, remains a
62 major hurdle. Recent years have seen numerous publications demonstrating the success of various processing
63 techniques for optical imagery of sea ice on limited test cases (e.g. Inoue et al., 2008; Kwok, 2014; Lu et al., 2010;
64 Miao et al., 2015; Perovich et al., 2002b; Renner et al., 2014; Webster et al., 2015). None of these techniques, however,
65 have been adopted as a standard or been used to produce large-scale datasets, and validation has been limited.
66 Furthermore, none have been challenged by imagery collected across the seasonal evolution of the ice or used to
67 process data from multiple sensor platforms. These issues must be addressed to enable in large scale production-type
68 image processing and use of high resolution imagery as a sea ice monitoring tool.

69 A unique aspect of high resolution sea ice imagery datasets, which differs from most satellite remote sensing, is
70 the quantity of image sources and data owners. Distributed collection and data ownership means centralized processing

Deleted: Inoue et al., 2008; Kwok, 2014; Lu et al., 2010; Miao et al., 2015; Perovich et al., 2002; Renner et al., 2014; Webster et al., 2015)

Deleted: conditions

75 of imagery to produce a single product is unlikely. Instead, we believe that distributed processing by dataset owners
76 is more likely and the community therefore has a substantial need for a shared, standard processing protocol.
77 Successful creation of such a processing protocol would increase imagery analysis and result in the production of
78 datasets suitable for ingestion by models to validate surface process parameterizations. In this paper, we assess
79 previous publications detailing image processing methods for remote sensing and present a novel scheme that builds
80 from the strengths and lessons of prior efforts. Our resulting algorithm, the Open Source Sea-ice Processing (OSSP)
81 Algorithm, is presented as a step toward addressing the community need for a standardized methodology, and released
82 in an open source implementation for use and improvement by the community.

83 We began with three primary design goals that guided our development of the image processing scheme. The
84 method must (1) have a fully automatic workflow and have a low barrier to entry for new users, (2) produce accurate,
85 consistent results in a standardized output format, and (3) be able to produce equivalent geophysical parameters from
86 a range of disparate image acquisition methods. To meet these goals, we have packaged OSSP in a user-friendly
87 format, with clear documentation for start-up. We include a set of default parameters that should meet most user needs,
88 permitting processing of pre-defined image types with minimal set-up. The algorithm parameters are tunable to allow
89 more advanced users to tailor the method to their specific imagery input. We chose an open source format to enhance
90 the ability for the community to explore and improve the code relative to a commercial software. Herein, we discuss
91 how we arrived at the particular technique we use, and why it is superior to some other possible mechanisms. We then
92 demonstrate the ability of this algorithm to analyze imagery of disparate sources by showing results from high
93 resolution DigitalGlobe WorldView satellite imagery in both panchromatic and pansharpened formats, aerial sRGB
94 (standard Red, Green, Blue) imagery, and NASA Operation IceBridge DMS (Digital Mapping System) optical
95 imagery. In this paper, we classify imaged areas into three surface types: Snow and ice, melt ponds and submerged
96 ice, and open water. The algorithm is, however, suitable for classifying any number of categories, should a user be
97 interested in different surface types, and might be adapted for use on imagery of other surface types.

98 **2 Algorithm Design**

99 Two core decisions were faced in the design of this image classification scheme: (1) Whether to analyze the image by
100 individual pixels or to analyze objects constructed of similar, neighboring pixels, and (2) which algorithm to use for
101 the classification of these image units.

102 Prior work [in terrestrial remote sensing applications](#) has shown that object-based classifications are more accurate
103 than single pixel classifications when analyzing high-resolution imagery (Blaschke, 2010; Blaschke et al., 2014; Duro
104 et al., 2012; Yan et al., 2006). In this case, 'high resolution' has a specific definition dependent on the relationship
105 between the size of pixels and objects of interest. An image is high resolution when surface features of interest are
106 substantially larger than pixel resolution and therefore are composed of many pixels. In such imagery, objects, or
107 groups of pixels constructed to contain only similar pixels (i.e. a single surface type), can be analyzed as a set. The m-
108 dm resolution imagery meets this definition for features like melt ponds and ice floes. Object based classification
109 enables an algorithm to extract information about image texture and spatial correlation within the pixel group;

110 information that is not available in single pixel based classifications and can enhance accuracy of surface type
111 discrimination. Furthermore, object based classifications are much better at preserving the size and shape of surface
112 cover regions. Classification errors of individual pixel schemes tend to produce a ‘speckled’ appearance in the image
113 classification with incorrect pixels scattered across the image. Errors in object based classifications, meanwhile,
114 appear as entire objects that are mislabeled (Duro et al., 2012). Since our intent is to process high-resolution imagery
115 and produce measurements not only of the areal fractions of surface type regions, but also to enable analysis of the
116 size and shape of ice surface type regions (e.g. for floe size or melt pond size determination), the choice of object
117 based classification over pixel based was clear.

118 A wide range of algorithms were considered for classifying image objects. We first considered the use of
119 supervised versus an unsupervised classification schemes. Unsupervised schemes were rejected as they produce
120 inconsistent, non-intercomparable results. These schemes, [such as clustering algorithms](#), group observations into a
121 predefined number of categories – even if not all feature types of interest are present in an image. For example, an
122 image containing only snow-covered ice will still be categorized into the same number of classes as an image with
123 snow, melt ponds, and open water together – resulting in multiple classes of snow. Since the boundary between classes
124 also changes in each image, standardizing results across imagery with different sources and of scenes with different
125 feature content would be challenging at best.

126 Supervised classification schemes instead utilize a set of known examples (called training data) to assign a
127 classification to unknown objects based on similarity to user-identified objects. Supervised classification schemes
128 have several advantages. They can produce fixed surface type definitions, allow for more control and fine tuning of
129 the algorithm, improve in skill as more points are added to the training data, and allow users to choose what surface
130 characteristics they wish to classify. While many machine learning techniques have shown high accuracy in remote
131 sensing applications (Duro et al., 2012), we selected a random forest machine learning classifier over other supervised
132 learning algorithms for its ability to handle nonlinear and categorical training inputs (Breiman, 2001; DeFries, 2000;
133 Pal, 2005), resistance to outliers in the training dataset (Breiman, 1996), and relative ease of implementation.

134 Our scheme, [learning from](#) the success of Miao et al. (2015) in classifying aerial imagery, uses an image
135 segmentation algorithm to divide the image into objects which are then classified with random forest machine learning.
136 [Our implementation of the segmentation and classification, however, were custom-built using well known image
137 processing tools \(Pedregosa et al., 2011; van der Walt et al., 2014\) in an open source format.](#) We do not attempt to
138 assert that our method is the optimal method for processing sea ice imagery. Instead, we argue that it is easily usable
139 by the community at large, produces highly accurate and consistent results, and merits consideration as a standardized
140 methodology. In coordination with this publication, we release our code (available at <https://github.com/wrightni>)
141 with the intention of encouraging movement toward a standardized method. Our hope is to continue development of
142 the algorithm with contributions and suggestions from the sea ice community.

Deleted: examples of which include K-means
Deleted: and maximum likelihood classifiers

Deleted: building on

146 **3 Methods**

147 **3.1 Image Collection and Preprocessing**

148 The imagery used to test the algorithm was selected from four distinct sources in order to assess the algorithm’s ability
149 to deliver consistent and intercomparable measures of geophysical parameters. We chose high resolution satellite
150 imagery from DigitalGlobe’s WorldView constellation in panchromatic and 8 band multispectral formats, NASA
151 Operation IceBridge Digital Mapping System optical imagery, and aerial sRGB imagery collected using an aircraft-
152 mounted standard DSLR camera as part of the SIZONet project. We first demonstrate the technique’s ability to handle
153 imagery representing all stages of the seasonal evolution of sea ice conditions on a series of 22 panchromatic satellite
154 images collected between March and August of 2014 at a single site in the Beaufort Sea: 72.0° N 128.0° W. We then
155 process 4 multispectral WorldView 2 images of the same site, each collected coincident with a panchromatic image
156 and compare results to assess the benefit of spectral information. Finally, we process a set of 20 sRGB images and 20
157 IceBridge DMS images containing a variety of sea ice surface types to illustrate the accuracy of the method on [aerial](#)
158 [image sources](#). The imagery sources chosen for this analysis were selected to be representative of the variation that
159 exists in optical imagery of sea ice, but there is an abundance of image data that can be processed with this technique.

Deleted: other image sources.

160 The satellite images were collected by tasking WorldView 1 and WorldView 2 Digital Globe satellites over fixed
161 locations in the Arctic. Tasking requests were submitted to DigitalGlobe with the support and collaboration of the
162 Polar Geospatial Center. The panchromatic bands of WorldView 1 and 2 both have a spatial resolution of 0.46m at
163 nadir. The WorldView 1 satellite panchromatic band samples the visible spectrum between 400 nm and 900 nm, while
164 the WorldView 2 satellite panchromatic band samples between 450 nm and 850 nm. In addition, WorldView 2 has 8
165 multispectral bands at 1.84 m nadir resolution, capturing bands within the range of 400nm to 1040nm. Each
166 WorldView image captures an area of ~700-1300 km². Of the 22 useable panchromatic collections at the site, 15 were
167 completely cloud free while 7 of the images were partially cloudy. Images with partial cloud cover were manually
168 masked and cloud covered areas were excluded from analysis. The aerial sRGB imagery was captured along a 100km
169 long transect to the north of Barrow, Alaska with a Nikon D70 DSLR mounted at nadir to a light airplane during June
170 2009. The IceBridge imagery was collected in July of 2016 near 73° N 171° W with a Canon EOS 5D Mark II digital
171 camera. We utilize the L0 (raw) DMS IceBridge imagery, which has a 10cm spatial resolution when taken from 1500
172 feet altitude (Dominguez, 2010, updated 2017).

173 Each satellite image was orthorectified to mean sea level before further processing. Orthorectification corrects for
174 image distortions caused by off-nadir acquisition angles and produces a planimetrically correct image that can be
175 accurately measured for distance and area. Due to the relatively low surface roughness of both multiyear and first year
176 sea ice (Petty et al., 2016), errors induced by ignoring the real topography during orthorectification are small.
177 Multispectral imagery was pansharpened to the resolution of the panchromatic imagery. Pansharpening is a method
178 that creates a high resolution multispectral image by combining intensity values from a higher resolution panchromatic
179 image with color information from a lower resolution multispectral image. The pansharpened imagery used here was
180 created using a ‘weighted’ Brovey algorithm. This algorithm resamples the multispectral image to the resolution of
181 the panchromatic image, then each pixel’s [value](#) is multiplied by the ratio of the corresponding panchromatic pixel

Deleted: vafue

184 value to the sum of all multispectral pixel values. The orthorectification and pansharpener scripts were developed by
185 the Polar Geospatial Center at the University of Minnesota and utilize the GDAL (Geospatial Data Abstraction
186 Library) image processing tools (GDAL, 2016). All imagery used was rescaled to the full 8-bit color space for
187 improved contrast and viewing. No other preprocessing was done to the aerial sRGB imagery or IceBridge DMS
188 imagery.

189 3.2 Image Segmentation

190 A flow chart of the image processing steps taken after pre-processing is presented in Fig. 2. The first task in the image
191 processing algorithm is to segment the image into groups of similar pixels, called objects. Accurate segmentation
192 requires finding the boundaries between the natural surface types we wish to differentiate (e.g. the boundary between
193 ice covered and open ocean), delineating their locations, and using these boundaries to produce image objects. Sea ice
194 surface types have large differences in reflectivity and tend to change abruptly, rather than gradually over a large
195 distance. We exploit this characteristic by using an edge detection algorithm to find boundaries between surface types.
196 Figure 3 contains a visual demonstration of this process. First, a Sobel-Feldman operator (van der Walt et al., 2014)
197 is applied to the input image (Fig. 3a). The Sobel-Feldman filter applies a discrete differentiation kernel across the
198 image to find the local gradient of the image intensity. High gradient values correspond to abrupt changes in pixel
199 intensity, which are likely boundaries between surface types. We scale the gradient values by an amplification factor
200 of 2 in order to further highlight edge regions in the image. Following the amplification, we threshold the lowest 10%
201 of the gradient image and set the values to zero. This reduces noise detected by the Sobel-Feldman filter, and eliminates
202 weaker edges. The amplification factor and gradient threshold percentage are both tuning parameters, which can be
203 adjusted to properly segment images based on the input image and the strength of edges sought.

204 The strongest edges in optical imagery of sea ice are typically the ocean-ice interface, followed by melt pond-ice
205 boundaries, then ice ridges and uneven ice surfaces. In general, the more edges detected, the more segmented the
206 image will become, and the more computational resources required to later classify the [increased number of](#) image
207 objects. On the other hand, an under-segmented image may miss the natural boundaries between surfaces. Under
208 segmentation introduces classification error because an object containing two surface types cannot be correctly
209 classified. An optimally segmented image is one which captures all the natural surface boundaries with minimal over-
210 segmentation (i.e. boundaries placed in the middle of features). The appropriate parameters for our imagery were
211 tuned by visual inspection of the segmentation results. In such inspection, desired segmentation lines are manually
212 drawn, and algorithm-determined segmentation lines are overlain and evaluated for completeness.

213 The result of the edge detection is a gradient map that marks the strength of edges in the image. We use a watershed
214 segmentation technique to build complete objects based on edge locations and intensity (van der Walt et al., 2014).
215 We first calculate all local minimum values in the gradient image, where a marker is then placed to indicate the origin
216 of watershed regions. Each region then begins iteratively expanding in all directions of increasing image gradient until
217 encountering a local maximum in the gradient image or encountering a separately growing region. This continues until
218 every pixel in the image belongs to a unique set. With the proper parameter selection, each object will represent a
219 single surface type. It is often the case that some areas will be over-segmented (i.e. a single surface feature represented

220 by multiple objects). Over segmentation can either be ignored, or objects can be recombined if they meet similarity
221 criteria in an effort to save computational resources. Here we chose to classify objects without recombination. Figure
222 3b shows the detected edges overlain on top of the input image.

223 The watershed segmentation algorithm benefits from the ability to create objects of variable size. Large objects
224 are built in areas of low surface variability while many small objects are created in areas of high variability. This
225 variable object sizing is well suited to sea ice surface classification because the variability of each surface type occurs
226 at different scales. Areas of open water and snow covered first year ice, for example, can often be found in large
227 expanses, while areas that contain melt ponds, ice ridges, or rubble fields frequently cover small areas and are tightly
228 intermingled with other surface types. Variable object sizes give the fine detail needed to capture surfaces of high
229 heterogeneity in their full detail, while limiting over segmentation of uniform areas.

230 3.3 Segment Classification

231 3.3.1 Overview

232 Once the image has been divided into regions of the same surface type, each object must be classified as to which
233 surface type it represents. We classify the objects using a random forest machine learning technique (Breiman, 2001;
234 Pedregosa et al., 2011). The development of a machine learning algorithm requires multiple iterative steps: 1) Select
235 attributes with which to classify each object, 2) create a training dataset, 3) classify unknown image objects based on
236 the training set, and 4) assess performance and refine, starting from step 1. Random forest classifiers excel for their
237 relative ease of use, flexibility in the choice of attributes that define each object, and overall high accuracy, even with
238 relatively small training datasets. The random forest classifier is only one of many available machine learning
239 approaches and others may also be suitable.

Deleted: .

240 3.3.2 Surface Type Definitions

241 Another key challenge to quantitatively monitoring sea ice surface characteristics from high resolution imagery is a
242 lack of standardized surface type definitions. We noted above that high-resolution sea ice imagery comes from many
243 sources; each with different characteristics. As we will see below, each image source will need to have its own training
244 set created by expert human classifiers. The human classifier must train the algorithm according to definitions of each
245 surface type that are broadly agreed upon in the community for the algorithm to be successful in producing
246 intercomparable datasets. While at first the definitions of open water, ice and melt ponds might seem intuitive, many
247 experts in the cryosphere community have differing opinions, especially on transitional states. Deciding where to
248 delineate transitional states is important to standardization. We have established the following definitions for the three
249 surface types we sought to separate, binning transitional states in a manner most consistent with their impact on albedo.

Deleted: challenge these notions

250 Our surface type definitions focus on the behavior of a surface in absorption of shortwave radiation and radiative
251 energy transfer. (1) Open Water (OW): Applied to surface areas that had zero ice cover as well as those covered by
252 an unconsolidated frazil or grease ice. (2) Melt Ponds and Submerged Ice (MPS): Applied to surfaces where a liquid
253 water layer completely submerges the ice. (3) Ice and Snow. Applied to all surfaces covered by snow or bare ice, as
254 well as decaying ice and snow that is saturated, but not submerged. The definition of melt ponds includes the classical

Deleted: (MP

Deleted: (I+S);

259 definition of melt ponds where meltwater is trapped in isolated patches atop ice, as well as optically-similar ice
260 submerged near the edge of a floe. [While previous work separates these categories \(e.g. \(Miao et al., 2015\) we did not](#)
261 [attempt to break these ‘pond’ types because the distinction is unimportant from a shortwave energy balance \(albedo\)](#)
262 [perspective](#). We further refined the ice and snow category into two sub categories: (3a) Thick Ice and Snow, applied
263 during the freezing season to ice appearing to the expert classifier to be thicker than 50cm or having an optically thick
264 snow cover and to ice during the melt season covered by a drained surface scattering layer (Perovich, 2005) of
265 decaying ice crystals and (3b) Dark and Thin Ice, applied during the freezing season to surfaces of thin ice that are not
266 snow covered including nilas and young ice. This label was also applied during melting conditions to ice covered by
267 saturated slush, but not completely submerged in water. This is ice which in some prior publications (e.g. Polashenski
268 et al., 2012) was labeled as ‘slushy bare ice’. We acknowledge that the boundary between the ice and snow sub-
269 categories is often more a continuum than a defined border but note that distinguishing the two types is useful for
270 algorithm accuracy. Dividing the [ice/snow](#) type creates two relatively homogeneous categories rather than a single
271 larger category with large internal differences. A user only interested in the categories of ice, ponds, and open water
272 could simply re-combine them, as we have done for analysis. [We created a temporary ‘shadow’ classification category](#)
273 [that was used only in panchromatic WorldView images captured prior to melt onset. This category allowed the](#)
274 [machine learning algorithm to differentiate dark shadows in spring imagery from melt ponds in summer imagery –](#)
275 [surface types that look similar in single-band imagery. This category is used exclusively as a temporary step in](#)
276 [processing that allows us to bypass masking shadow regions directly \(e.g. \(Webster et al., 2015\). As this is not](#)
277 [designed to be a standalone classification category \(as opposed to Miao et al., 2015, 2016\), objects classified as a](#)
278 [shadow were grouped back with the ice/snow category.](#)

Deleted: We did not attempt to break these ‘pond’ types because the distinction is unimportant from a shortwave energy balance (albedo) perspective.

Deleted:

Deleted: I+S

Deleted: Furthermore, we

Deleted: classification

Deleted: based on single-band pixel intensity values. The shadow category was grouped back with the I+S category for analysis.

279 3.3.3 Attribute Selection

280 Attributes are quantifiable measures of image object properties used by the classifier in discriminating surface types.
281 An enormous array of possible attributes could be calculated for each image object and could be calculated in many
282 ways. Examples of properties that could be quantified as attributes include values of the enclosed pixels, the size and
283 shape of the object, and values of adjacent pixels. The calculation of pixel values aggregated by image objects takes
284 advantage of the additional information held in the pixel group (as compared to individual pixels). We have compiled
285 a list representing a relevant subset of such attributes that can be used to distinguish different surface types in Table
286 1. We included a selection of attributes similar to those used in previous publications (e.g. Miao et al., 2015), as well
287 as attributes we have developed specifically for our algorithm.

288 Each image source provides unique information about the surface and it can be expected that a different list of
289 attributes will be optimal for classification of each image type – even though we seek the same geophysical parameters.

290 [As high-resolution satellite images can have millions of image objects, calculating the attributes of each object quickly](#)
291 [becomes](#) computationally expensive. We have, therefore, determined those that are most valuable for classifying each
292 image type to use in our classification. For example, pansharpened WorldView 2 imagery has 8 spectral bands which
293 can inform the classification, while panchromatic versions of the same image have only a single band. Our goal was
294 to select a combination of attributes that describe the intensity and textural characteristics of the object itself, and of

Deleted: Calculating

Deleted: image

Deleted: is

307 the area surrounding the object. Table 1 indicates which attributes were selected for use in classifying each image
308 type.

309 We selected attributes by only including those with a high relative importance. The importance of each attribute
310 is a property of a random forest classifier, and is defined as the number of times a given attribute contributed to the
311 final prediction of an input. After initial tests with large numbers of attributes, we narrowed our selection by using
312 only those attributes that contributed to a classification in greater than 1% of cases. For discussion here, we group the
313 attributes into two broad categories: Those calculated using internal pixels alone (object attributes), and those
314 calculated from external pixel values (neighbor attributes).

315 3.3.4 Object Attributes

316 The most important attributes in the classification of an image segment were found to be aggregate measures of pixel
317 intensity within the object. We determine these by analyzing the mean pixel intensity of all bands and the median of
318 the panchromatic band. An important benefit of image segmentation is the ability to calculate estimates of surface
319 texture by looking at the variability within a group of pixels. The texture is often unique in the different surface types
320 we seek to distinguish. Open water is typically uniformly absorptive and has minimal intensity variance. Melt ponds,
321 in contrast, come in many realizations and exhibit a wider range in reflectance, even within individual ponds. To
322 estimate surface texture, we calculate the standard deviation of pixel intensity values and the image entropy within
323 each segment. Image entropy, H , is calculated as

$$324 H = - \sum p * \log_2 p$$

325 where p represents the bin counts of a pixel intensity histogram within the segment. We also calculate the size of each
326 segment as the number of pixels it contains. As sea ice surface characteristics evolve appreciably over time,
327 particularly before and after melt onset, we use image acquisition date as an attribute in for classification. While date
328 of melt onset varies, and the reader might argue that a more applicable attribute would be image melt state, melt state,
329 is not an a priori characteristic of the image. It would therefore need to be manually defined, and not meet our demand
330 for a fully automated scheme.

331 In multispectral imagery, we also calculate the ratios between the mean absorption of each object in certain
332 portions of the spectrum. The important band ratios used for the multispectral WorldView imagery were determined
333 empirically. We tested every possible band combination, and successively removed the ratios that did not contribute
334 to more than 1% of object classifications. In sRGB imagery we use the band ratios shown to be informative in this
335 application by Miao et al. (2015).

336 In addition to information contained within each object, we utilize information from the surrounding area. To
337 analyze the surrounding region, we determine the dimensions of a minimum bounding box that contains the object,
338 then expand the box by five pixels in each direction. All pixels contained within this box, minus those in the object,
339 are considered to be neighboring pixels. Analogous to the internal attribute calculations, we find the average intensity
340 and standard deviation of these pixels. We also calculate the maximum single intensity within the neighboring region.
341 Searching for attributes outside of the object improves the algorithm's predictive capabilities by providing spatial
342 context. Bright neighboring pixels (as an analog for an illuminated ridge) often provide information to distinguish, for

Deleted: We include image date as an attribute because

Deleted: pond formation

Deleted: . Since

Deleted: . Melt

Deleted: however,

Deleted: and

Deleted: therefore

Deleted: meeting

Deleted: segment

Deleted: segment

Deleted: 3.3.5 Neighbor Attributes .

Deleted: segment

Deleted: segment

Deleted: segment

Deleted: this

Deleted: , which measures

Deleted: the presence

Deleted: neighboring

Deleted: . The maximum neighboring intensity

Deleted: provides

363 example, a shadowed ice surface from a melt pond. In panchromatic imagery, [melt ponds and shadows appear](#) similar
364 when evaluated solely on internal [object](#) attributes. [However, a dark region with an immediately adjacent bright region](#)
365 [is more likely to be a shadow than a dark region not adjacent to a bright pixel \(e.g. a pond\)](#). We do note that it is likely
366 that a more complex algorithm, for example identifying those pixels in a radius or distance to the edge of the segment,
367 rather than using a bounding box, would be more reliable. The tradeoff, however, is one of higher computational
368 expense.

Deleted: these regions are often

Deleted: segment

369 3.4 Training Set Creation

370 Four training datasets were created to analyze the images selected for this paper. One training set was created for
371 each imagery source: Panchromatic satellite imagery, multispectral satellite imagery, aerial sRGB imagery, and
372 IceBridge DMS imagery. Each training set consists of a list of image objects that have been manually classified by a
373 human and a list of attribute values calculated from those objects and their surroundings. The manual classification is
374 carried out by multiple sea ice experts. Experienced observers of sea ice can classify the majority (85%+) of segments
375 in a high resolution optical image with confidence. To address the ambiguity in correct identification of certain
376 segments, however, we used several (4) skilled sea ice observers to repeatedly classify image objects. For the initial
377 creation of our training datasets, two of the users had extensive training in the OSSP algorithm and surface type
378 definitions, while the other two [no experience with the algorithm](#). [Users in both categories were briefed on the standard](#)
379 [surface type definitions used for this study \(section 3.3.2\)](#). Figure 4 shows a confusion matrix to compare user
380 classifications. Cells in the diagonal indicate agreement between users, while off-diagonal cells indicate disagreement
381 [\(Pedregosa et al., 2011\)](#). Agreement between the two well-trained users was high (average 94% of segment
382 identifications; Fig. 4a), while the agreement between a well-trained user and a new user was lower (average of 86%;
383 [Fig 4b](#)). After an in-person review of the training objects among all four users, the overall agreement rose to 97%. The
384 remaining 3% of objects were cases where the expert users could not agree on a single classification, even after review
385 of the surface type definitions and discussion. These objects were therefore not used in the final training set. Figure 5
386 shows a series of surface types that span all our classification categories, including those where the classification is
387 clear and those where it is difficult. Difficult segments are over-represented in these images for illustrative purposes,
388 and represent a relatively small fraction of the total surface.

Deleted: had only a brief (i.e. <10 minute) introduction to the surface type definitions and

Deleted: (Pedregosa et al., 2011)

Deleted: ig

389 While the skill of the machine learning prediction increases substantially as the size of the training set grows,
390 creating large training sets is time consuming. We found that training datasets of approximately 1000 points yielded
391 accurate and consistent results. We have developed a graphical user interface (GUI) to facilitate the rapid creation of
392 large training sets (see Fig. 6). The GUI presents a user with the original image side by side with an overlay of a single
393 segment on that image. The user assigns a classification to the segment by visual determination.

394 The training dataset is a critical component of our algorithm because it directly controls the accuracy of the
395 machine learning algorithm – and using a consistent training set is necessary for producing intercomparable results.
396 In coordination with this publication we are releasing our version 1.0 training datasets with the intention that they
397 would represent a first version of *the* standard training set to use with each image type. Though we have found this

404 training dataset robust through our error analyses below, it is our intention to solicit broader input from the community
405 to refine and expand the training datasets available and release future improved versions.

406 In addition to cross-validating the creation of a training dataset between users, we assess the quality of our training
407 set through an out-of-bag (OOB) estimate, which is an internal measure of the training set's predictive power. The
408 random forest method creates an ensemble (forest) of classification trees from the input training set. Each classification
409 tree in this forest is built using a random bootstrap sample of the data in the training set. Because training samples are
410 selected at random, each tree is built with an incomplete set of the original data. For every sample in the original
411 training set, there then exists a subset of classifiers that do not contain that sample. The error rate of each classifier
412 when used to predict the samples that were left out is called the OOB estimate (Breiman, 2001). The OOB estimate
413 has been shown to be equivalent to predicting a separate set of features and comparing the output to a known
414 classification (Breiman, 1996).

415 3.5 Assigning Classifications

416 Once the training dataset is complete, the algorithm is prepared to predict the classification of unknown objects in the
417 images. The random forest classifier is run and a classified image is created by replacing the values within each
418 segment by the classification label predicted. Figure 3c shows the result of labeling image objects with their predicted
419 classification. From the classified image, it is possible to produce a number of useful statistics. The most basic
420 measurement is the total pixel counts for each of the three surface categories. This provides both the total area, in
421 square kilometers, that each surface covers, and the fraction of each image that is covered by each surface type. It
422 would also be possible to calculate measurements such as the average segment size for each surface, melt pond size
423 and connectivity, or floe size distributions. Each of these, however, has its own standardization problems significant
424 enough to merit their own paper.

425 For demonstration, we have used the output from our image classification to calculate the fractional melt pond
426 coverage for each date. The melt pond fraction was defined as the area of melt ponds [and submerged ice](#) divided by
427 the total area covered by ice floes, i.e.:

$$428 \text{ Melt Pond Coverage} = \frac{\text{Area}_{MPS}}{\text{Area}_{MPS} + \text{Area}_{I+S}}$$

429 where the subscript [MPS](#) indicates predicted melt ponds [and submerged ice](#) and I+S indicates predicted ice and snow.

430 3.6 Determining Classification Accuracy

431 The primary measure of classification accuracy was to test the processed imagery on a per pixel basis against human
432 classification. For [every](#) processed image, we selected a simple random sample of 100 pixels [chosen from the whole](#)
433 image and asked four sea ice experts to assign a classification to those pixels. [For a single image from](#) each image
434 source, we also [asked the sea ice experts to classify and additional 900 pixels](#). [This](#) larger sample was created to
435 demonstrate a tighter confidence interval, while the smaller samples were chosen to demonstrate consistency across
436 images. [We used the same GUI developed to create training datasets to assess pixel accuracy](#). Pixels were presented
437 [at random](#) to the user by showing the original image with the given pixel highlighted. The [user](#) then identified which

Deleted: $Area_{MP}$

Deleted: MP

Deleted: MP

Deleted: each

Deleted: entire

Deleted: Note that in this case experts are asked to classify individual pixels, rather than segments as they were asked to do in training set creation. For

Deleted: ,

Deleted: selected one scene from which to check

Deleted: classification of a larger sample of 1000

Deleted: The

Deleted: in the accuracy

Deleted: This metric gives a spatially weighted accuracy by assessing individual pixels regardless of how the image was segmented. The pixels

Deleted: observer

455 of the surface type categories best described that pixel. This assignment is then compared to the algorithm's prediction
456 behind the scenes. The accuracy, as determined by each of the four experts, was averaged to create a composite
457 accuracy for each image.

- Deleted: three
- Deleted: without feedback to
- Deleted: human classifier.
- Deleted: observers

458 4 Results

- Deleted:

459 4.1 Classification of Four Imagery Sources

460 The OSSP image processing method proved highly suitable for the task of classifying sea ice imagery. A visual
461 comparison between the raw and processed imagery, shown in Fig. 7 can quickly demonstrate this in a qualitative
462 sense. Figure 7 contains a comparison between the original and classified imagery for each source, selected to show
463 the performance of the algorithm on images that contain a variety of surface types. The colors shown correspond to
464 the classification category; regions colored black are open water, blue regions are melt ponds and submerged ice, gray
465 regions are wet and thin ice, and white regions are snow and ice. The quantitative processing results, including surface
466 distributions and classification accuracy are shown in Table 2. The overall classification accuracy was $96 \pm 3\%$ across
467 20 IceBridge DMS images; $95 \pm 3\%$ across 20 aerial sRGB images; $97 \pm 2\%$ across 22 panchromatic WorldView 1
468 and 2 images; and $98 \pm 2\%$ across 4 multispectral WorldView 2 images.

- Deleted: two comparisons
- Deleted: imagery

469 The nature of the classification error is presented using a confusion matrix that compares the algorithm
470 classification with a manual classification for 1000 randomly selected pixels. Four confusion matrices, one for a single
471 image from each of the four image sources is shown in Fig. 8. Values along the diagonal of the square are the
472 classifications where the algorithm and the human observer agreed, while values in off-diagonal areas indicate
473 disagreement. Concentration of error into a particular off-diagonal cell helps illustrate the types of confusion the
474 algorithm experiences. The number of pixels that fall into off-diagonal cells is low across all imagery types. In the
475 IceBridge imagery, there is a slight tendency for the algorithm to classify surfaces as open water where a human would
476 choose melt pond. This is caused by exceptionally dark melt ponds on the edge of melting through (Fig. 5, panels F
477 and I). Classification of multispectral WorldView imagery has a small bias towards classifying melt ponds over dark
478 or thin ice (Fig. 5, panel D). Aerial sRGB and Panchromatic WorldView images do not have a distinct pattern to their
479 classification errors.

- Deleted: of
- Deleted: One
- Deleted: matrix is shown in Fig. 8

480 The internal metric of classification training dataset strength, the Out of Bag Error (OOB) estimates, on a 0.0 to
481 1.0 scale, are shown in Table 3 for the trees built from our three training sets. The OOB estimate represents the mean
482 prediction error of the random forest classifier, i.e. an OOB score of 0.92 estimates that the decision tree would predict
483 92% of segments that are contained in the training dataset correctly. The discrepancy between OOB error and the
484 overall classification accuracy is a result of more frequent misclassification of smaller objects; overall accuracy is area
485 weighted, while the OOB score is not.

486 4.2 WorldView: Analyzing A Full Seasonal Progression

- Deleted: 1

487 We analyzed 22 images at a single site in the Beaufort Sea collected between March and August of 2014 to challenge
488 the method with images that span the seasonal evolution of ice surface conditions. The site is Eulerian; it observes a

- Deleted: The

501 [single location in space rather than following a single ice floe through its lifecycle as it drifts](#). Still, the results of these
502 image classifications (shown in Fig. 9) illustrate the progression of the ice surface conditions in terms of our four
503 categories over the course of a single melt season. While cloud cover impacted the temporal continuity of satellite
504 images collected at this site, we are still able to follow the seasonal evolution of surface features. A time series of
505 fractional melt pond coverage calculated from the satellite image site is plotted in Fig. 10. The melt pond coverage
506 jumps to 22% in the earliest June image, as initial ponding begins and floods the surface of the level first year ice.
507 This is followed by a further increase to 45% coverage in the next few days. The melt pond coverage then drops back
508 down to 30% as melt water drains from the surface and forms well defined ponds. The evolution of melt pond coverage
509 over our satellite observation period is consistent with prior field observations (Eicken, 2002; Landy et al., 2014;
510 Polashenski et al., 2012) and matches the four stages of ice melt first described by Eicken (2002). The ice at this
511 observation site fully transitions to open water by mid-July, though it appears that the ice is advected out of the region
512 in the late stages of melt rather than completing melt at this location.

513 5 Discussion

514 5.1 Error

515 There are four primary sources of error in the OSSP method as presented, two internal to the method and two external.
516 Internal error is caused by segment misclassification and by incomplete segmentation (i.e. leaving pixels representing
517 two surface types within one segment). The net internal error was quantified in section 3.6 and 4. External error is
518 introduced by pixilation – or blurring of real surface boundaries due to insufficient image resolution – and human
519 error in assigning a ‘ground truth’ value to an aerial or satellite observation during training.

520 5.1.1 Internal Error

521 Through assessing the accuracy of each classified image on a pixel-by-pixel basis (section 3.6), we collect all internal
522 sources of error into one measurement: The algorithm either [assigned the same classification as a human would have](#),
523 or it did not. Total internal accuracy calculated for the method, relative to human classifiers, is quite good, at 90-99%
524 across all image types. Our experience is that this level of accuracy approaches the accuracy with which fractional
525 surface coverage can practically be determined from labor intensive ground campaign techniques such as lidar and
526 measured linear transects (e.g. Polashenski et al., 2012)

527 [The first type of internal error is misclassification error, where the image classification algorithm fails to assign](#)
528 [the same classification that a human expert would choose](#). This type of error is best quantified by analyzing the training
529 datasets. The OOB score for each forest of decision trees (Table 3) provides an estimate of each forest’s ability to
530 correctly predict objects similar to those used to create the forest (section 3.4). The OOB score is not influenced by
531 segmentation error, because the objects selected for training dataset use were filtered to remove any objects that
532 contained more than one surface type. The most commonly misapplied category was the Dark and Thin Ice
533 subcategory of Ice and Snow. This category often represents surface types that are in a transitional state, and is often
534 difficult to classify even for a human observer.

Deleted: classified each pixel

Deleted: way

Deleted: the

Deleted: Misclassification error, the

Deleted: occurs when

Deleted: replicate the

Deleted: experts’ decision-making process

542 [The second type of internal error is segmentation error, where](#) an object is created that contains more than one of
543 the surface types we are trying to distinguish. This occurs when boundaries between objects are not placed where
544 boundaries between surfaces exist; an issue most common where one surface type gradually transitions to another.
545 When this occurs, some portion of that object will necessarily be misclassified. We have compensated for areas that
546 lack sharp boundaries by biasing the image segmentation towards over-segmentation, but a small number of objects
547 still contain more than one surface type. During training set creation, we asked the human experts to identify objects
548 containing more than one surface type. 3.5% of objects were identified as insufficiently segmented in aerial imagery,
549 and 2% of objects in satellite imagery. This represents the upper limit for the total percentage of insufficiently
550 segmented objects for several reasons. First, segmentation error was most prevalent in transitional surface types (i.e.
551 Dark and Thin Ice), which represents a small portion of the overall image and is composed of relatively small objects.
552 This category is overrepresented in the training objects because objects were chosen to sample each surface type and
553 not weighted by area. In addition, insufficiently segmented objects are generally composed of only two surface types,
554 and end up identified as the surface which represents more of the object's area. Hence the total internal error introduced
555 by segmentation error is appreciably smaller than misclassification error, likely well under 1%.

556 5.1.2 External Error

557 The first form of external error is introduced by image resolution. At lower image resolutions, more pixels of the
558 image span edges, and smaller features are more likely to go undetected. Pixels on the edge of surface types necessarily
559 represent more than one surface type, but can be classified as only one. Misclassification of these has the potential to
560 become a systemic error if edge pixels were preferentially placed in a particular category. We assessed this error's
561 impact by taking high resolution IceBridge imagery (0.1m), downsampling to progressively lower resolution, and
562 reprocessing. Figure 11 shows the surface type percentages for three IceBridge images at decreasing resolution. Figure
563 12 shows a series of downsampled images and their classified counterparts. Surprisingly, despite clear pixilation and
564 aliasing in the imagery, little change in aggregate classification statistics occurred as resolution was lowered from 0.1
565 to 2m. This suggests that at resolutions used for this paper, edge pixels do not significantly impact the classification
566 results. It may also be possible to forego the pansharpening process discussed in section 3.1, and use 2m multispectral
567 WorldView imagery directly.

568 The second type of external error occurs when the human expert fails to correctly label a segment. Even skilled
569 human observers cannot classify every pixel in the imagery definitively, and indeed the division between the surface
570 types can sometimes be indistinct even to an observer on the ground. We addressed this concern by employing
571 observers extensively trained in the sea ice field, both in remote sensing and in-situ observations, comparing multiple
572 human classifications of the same segments. After discussion, the portion of image objects subject to human observer
573 disagreement or uncertainty is small. Human observers disagreed on 3% of objects creating our training sets. The
574 possibility of systemic bias among the expert observer classifications cannot be excluded because real ground truth,
575 in the form of geo-referenced ground observations from knowledgeable observers was, unfortunately, not available
576 for any of the imagery. Conducting this type of validation would be helpful, but given high confidence human expert
577 classifiers expressed in their classifications and low disagreement between them, may not be essential.

Deleted: Segmentation error, the

Deleted: ,

Deleted: caused when

581 **5.1.3 Overall Error**

582 The fact that misclassification dominates the internal error metric suggests that error could be reduced if additional
583 object attributes used by human experts to differentiate surface types could be identified. The agreement between the
584 OSSP method and a human (96%+/-3%) is similar to the agreement between different human observers (97%),
585 meaning that the algorithm is nearly as accurate as a human manually classifying an entire image. If we exclude the
586 possibility for systemic error in human classification, and assume other errors are unrelated to one another, we can
587 calculate a total absolute accuracy in surface type determination as approximately 96%.

588 **5.2 Producing Derived Metrics of Surface Coverage**

589 The classified imagery, presented as a raster, (e.g. Fig. 7) is not likely to be the end product used in many analyses.
590 Metrics of the sea ice state in simpler form will be calculated. We already introduced the most basic summary metrics
591 in section 4, where we presented fractional surface coverage calculated from the total pixel counts for each of the four
592 surface categories in each image. We also presented the calculation of melt pond coverage as a fraction of the ice-
593 covered portion of the image, rather than total image area. The calculation of these is straightforward. Other metrics
594 commonly discussed in the literature that could be produced with minimal additional processing include those
595 capturing melt pond size, connectivity, or fractal dimension, as well as floe size distribution or perimeter to area ratio.
596 As with definitions of surface type, standardizing metrics will be necessary to produce intercomparable results. We
597 discussed the more complex metrics which could be derived from this imagery with several other groups. We
598 determined that standardizing these and other more advanced metrics will require more input and consensus building
599 before a community standard can be suggested. We leave determining standard methods for calculating these more
600 complex metrics to a future work.

601 Equipped with the images processed by OSSP, we consider what size area must be imaged, classified, and
602 summarized to constitute ‘one observation’ and how regionally representative such an observation is. Even with the
603 increasing availability of high resolution imagery, it is unlikely that high resolution imaging will regularly cover more
604 than a small portion of the Arctic in the near future. As a result, high resolution image analysis will likely remain a
605 ‘sampling’ technique. Since the scale of sea ice heterogeneity varies for each property type, a minimum area unique
606 to that property must be analyzed to qualify as a representative sample of the surface conditions. Finding that minimum
607 area involves addressing the ‘aggregate scale’ – the area over which a measured surface characteristic becomes
608 uniform and captures a representative average of the property in the area (Perovich, 2005). It may also be possible to
609 determine an aggregate scale statistic within well constrained bounds by random sub-sampling of the region, and
610 therefore reduce processing time. Here we conduct analysis of these sampling concepts and suggest this analysis of
611 the aggregate scale be conducted for any metric.

612 First, we sought to determine the aggregate scale for the simple fractional coverage metrics of ice as a fraction of
613 total area and melt pond as a fraction of ice area. This would inform us, for example, as to whether processing the
614 entire area of a WorldView image (up to 1000km²) was necessary, or alternatively if a full WorldView image was
615 sufficient to constitute a sample. First, we evaluated the convergence of fractional coverage within areas of increasing
616 size towards the image mean. For a WorldView image depicting primarily first year ice in various stages of melt, we

- Deleted:** ;
- Deleted:** ; and ridged ice coverage or frequency
- Deleted:** For this general work
- Deleted:** felt that more important than the specific definition of additional metrics of surface heterogeneity, is the consideration of what
- Deleted:** for
- Deleted:** to be collected
- Deleted:** Similarly, it
- Deleted:** sub-sample within a representative area and
- Deleted:** the mean of
- Deleted:** sample
- Deleted:** , reducing
- Deleted:** this area
- Deleted:** Equipped with the images processed by OSSP
- Deleted:** first
- Deleted:** for ice
- Deleted:** coverage (
- Deleted:**).
- Deleted:** worldview
- Deleted:** (~
- Deleted:** worldview
- Deleted:** We did this by evaluating
- Deleted:** feature
- Deleted:** image
- Deleted:** to a regional
- Deleted:** each
- Deleted:** acquired during the melt season, we determined the fractional
- Deleted:** pond and ice coverage within

647 created non-overlapping gridded subsections, and determined the fractional coverage within each grid cell. The size of
648 grid cells was varied logarithmically from 100 x 100 pixels (10^2) to 31622x31622 pixels ($10^{4.5}$) or from 0.0025km² to
649 250km². For each sample size, we gridded the image and evaluated every subsection within the entire image. Figure
650 13a shows a scatterplot of the fractional melt pond coverage in each image grid plotted against the log of total area of
651 that grid cell. As the area sampled increases, the melt pond fraction shows lower deviation from the mean, as expected.
652 To assist in evaluating the convergence towards the mean, we plot the 95% prediction interval for each image subset
653 size in Fig. 13a (large red dots). The range of pond fraction values between these two points represents the interval
654 within which 95% of samples of this size would fall. The width of the 95% prediction interval declines linearly with
655 respect to sample area in log space, shrinking by 0.3 for each order of magnitude that sample area increases. Visually,
656 it appears that maximum convergence may have been reached at a sample area of ~30km² (~ $10^{1.5}$ km²), though there
657 are an insufficient number of samples at this large area, within a single image to be certain. Regardless of whether
658 convergence is complete, the prediction interval tells us that at 30km², 95% of areas sampled could be expected to
659 have pond coverage within 5% of the mean of a full image (~1000km²). This is consistent with prior work that
660 indicated the aggregate scale for melt pond fraction determination is on the order of several tens of square kilometers
661 (Perovich, 2005; Perovich et al., 2002a). In Fig. 13b we conduct the same analysis for the total ice-covered fraction
662 (ponded + unponded ice) of the image. We see the range of the prediction interval generally drops as larger samples
663 are taken, but does not converge as cleanly or quickly as the pond coverage prediction interval does - a finding that is
664 unsurprising as ice fraction is composed of discrete floes with sizes much larger than melt ponds. The limited
665 convergence indicates that the aggregate scale for determination of ice covered fraction is at least on the order of the
666 scale of a WorldView image, and likely larger. Aggregate scale ice concentration, unlike melt pond fraction, is a
667 statistic better observed with medium resolution remote sensing platforms such as MODIS or Landsat due to the need
668 for a larger satellite footprint. WorldView imagery may be particularly useful for determining smaller scale parts of
669 floe size distributions or for validating larger scale remote sensing of ice fraction, if the larger scale pixels can be
670 completely contained within the worldview image. Floe size distribution will likely require nesting of scales in order
671 to fully access both large and small-scale parts of the floe size distribution.

672 We next investigated whether it is possible to reduce the processing load required to determine the melt pond or
673 ice fraction of an image within certain error bounds by processing collections of random image subsets. To do this, it
674 is useful to first establish two definitions: (1) one random sample of size N represents N randomly selected 100x100
675 pixel boxes, and (2) one adjacent sample of size N is a single area with size $100\sqrt{N} \times 100\sqrt{N}$. In other words, a
676 random sample and an adjacent sample both represent an image area of $10,000 * N$ pixels, but consist of independent
677 and correlated pixels, respectively. We expect random samples to better represent the total image mean melt pond
678 fraction because ice conditions are spatially correlated and a single large area is not composed of independent samples.
679 We evaluated this hypothesis by collecting 1000 random and adjacent samples of size $N=100$, with replacement.
680 Results are shown in Fig. 14. In Figure 14a, we plot a histogram of the mean melt pond fraction determined from these
681 1000 samples. The means determined from sets that contained randomly distributed image areas, are in red. The means
682 determined from sets of adjacent image areas are in blue. Although both sets represent samples of the same total image

Deleted: .
Deleted: subsections
Deleted: subsample
Deleted: for fractional surface coverage.
Deleted: 10
Deleted: determined from
Deleted: subset
Deleted: ice and pond
Deleted: in the image subset.
Deleted: determined from independent sample areas within the overall image
Deleted: toward
Deleted: size
Deleted: with a slope of approximately 0.3 across most of the range in sample area size explored. In other words, the prediction interval declines in width
Deleted: the
Deleted: is increased by. It
Deleted: or nearly reached
Deleted: we have
Deleted: size
Deleted: this
Deleted: scale
Deleted: image
Deleted: , and indicates that imagery representing an area as little as 3% of a Worldview image can provide an estimate of melt pond fraction that is representative of the mean at 1000km ² scale within what may be tolerable limits for many applications. In Fig. 13b we conduct the same analysis, only this time for
Deleted: since the
Deleted: (We limit prediction interval to the range 0-1.)
Deleted: further
Deleted: In
Deleted: case, the idea
Deleted: collect a large number of
Deleted: of from an image, instead of a single, larger sample of the same area as the sum of the smaller random samples. We expected the random samples will
Deleted: overall
Deleted: the
Deleted: larger
Deleted: Namely, ice conditions are spatially correlated.
Deleted: processing sets of 100 image subsamples representing both adjacent and randomly selected image areas.
Deleted: 1000 sets of image areas. Each of the sets contained 100 sample areas of 100x100 pixels. The means determined from sets that contained adjacent image areas, essentially representing a single image sample 10 times larger in area, are in blue.
Deleted: selected
Deleted: Though

733 area, the one composed of independent subsets randomly selected from across the image does a much better job of
734 representing the mean value, with a smaller standard deviation.

735 Estimating the mean of a complete image by sampling randomly selected areas of the image becomes a simple
736 statistics problem. The sample size needed to estimate a population mean to within a certain confidence interval and
737 margin of error can be determined with the formula:

738
$$n = \left(\frac{Z\sigma}{ME}\right)^2$$

739 where n is the sample size, Z is the z-score for the confidence interval required, σ is the population standard deviation,
740 and ME is the margin of error. The standard deviation of random samples with size 100 is ~0.2 (Fig 14b). Assuming
741 a 95% confidence interval ($Z=1.96$), and a margin of error of 5%, a sample size of 64 is required. In other words, with
742 64 random samples of size 100 we can predict the mean melt pond fraction of the total image with 95% confidence to
743 within 5%. 64 samples of size 100 corresponds to an image area of ~16km², significantly smaller than the total image
744 size.

745 In order to show these results visually, we return to Fig. 13 and place another set of 95% prediction interval bounds
746 (purple dots). These bounds represent the prediction interval for a random sample of size necessary for the total area
747 to equal the area on the x axis. The result is quite powerful. By processing as little as 16km² of the image, collected
748 from samples randomly distributed across the area, we can determine aggregate melt pond fraction to within 5% of
749 the true value with a confidence of 95%. We estimate that this 5% margin of error is comparable to the sum of internal
750 (2-4%) and external errors in our processing algorithm (section 5.1). For large scale processing we suggest that when
751 the sample confidence interval is below the image processing technique accuracy, sampling of larger areas is no longer
752 necessary.

753 A similar analysis is presented in Fig. 14c and 14d for ice fraction. While the WorldView image is likely not large
754 enough to represent the aggregate scale for ice fraction, randomly sampling the image still provides an expedient way
755 to determine the mean ice fraction of the image within certain bounds, while processing only a small fraction of the
756 image. Calculating the 95% prediction interval of random samples representing the total image area shown on the x
757 axis (purple dots) again shows that the total image mean can be estimated by calculating only a small portion of the
758 total image.

759 These explorations of image sampling permit us to recommend that users can estimate the total image pond fraction
760 by selecting N sets of 100 randomly selected 50x50m regions (where N is selected to provide the desired confidence
761 interval and margin of error). We suggest a standard, which incorporates some 'safety factor', for processing imagery
762 to produce estimates of melt pond fraction should be to process 25km² of area contained in at least 100 randomly
763 located image subsets from domains of at least 100km². We note that flying a UAV over a domain and collecting
764 imagery along flight tracks will not count as fully 'random' in this context, since the images along-track are spatially
765 correlated. Since an image does not represent the aggregate scale for ice fraction, we cannot recommend a specific
766 sampling strategy for the aggregate scale, but note that processing of 25km² of imagery from randomly distributed
767 subsets produces a prediction interval around the mean of approximately the same size as the upper limit of uncertainty
768 for our image processing technique. The statistical approach for determining aggregate statistics should not depend

Deleted: Figure 14b shows the standard deviation for the same image sets. Independent samples from across the image show a lower range in lower standard deviation within the image sets as well, though the average standard deviation is slightly higher. Again, this is expected, given the strong spatial correlation of surface coverage fraction within the images

Deleted: We next test the central limit theorem to see how well we can predict the error bounds from processing a single set of independent (i.e. randomly distributed) samples. The central limit theorem states that when taking the mean of a sufficiently large number of independent samples of a random variable, the standard error of the mean of the samples is equal to $\frac{\sigma}{\sqrt{N}}$ where σ is the standard deviation of the sample values and N is the sample size. The standard deviation of pond coverage fraction in sets of 100 sub-images ranged from 0.15 to 0.25 across the 1000 sample sets run (see histogram in Fig. 14b) This yields a predicted standard error of the mean determined from any one of these sets of 0.015 to 0.025 [1]

Deleted: Fig. 13

Deleted: now

Deleted: , this time representing twice the standard error [2]

Deleted: 100 randomly distributed sub-areas that total

Deleted: We show that

Deleted: a relatively small fraction

Deleted: area, so long as that sub-area is

Deleted: a large number of

Deleted: permits expedient determination of melt pond fraction [3]

Deleted: scale. In this case, processing as little as 5km² (~0.05 of the total area) [4]

Deleted: determined for the entire image. We estimate that

Deleted: determined melt pond fraction is

Deleted: reasonable

Deleted: of

Deleted: .

Deleted: ,

Deleted: 95% prediction

Deleted: (sampling error)

Deleted: well

Deleted: worthwhile

Deleted: A test of the central value theorem again shows that [5]

Deleted: that can be expected for image sets containing 100

Deleted: that

Deleted: the

Deleted: , with some safety factor built in,

Deleted: must process imagery representing at least 5km² if [6]

Deleted: located subsets from domains of at least 30 km²

Deleted: produce an 'aggregate scale' estimate

Deleted: pond coverage.

Deleted: 10km²

Deleted: 5km²

Deleted: 100

Deleted: These

849 [on the seasonality of the image nor the type of image used so long as the total area observed is sufficiently greater](#)
850 [than the variability in the surface feature being investigated. However, these](#) recommendations should be considered
851 provisional, because they are subject to impacts from differences in ice property correlation scales, and should be
852 further evaluated for accuracy as larger processed datasets are available.

853 5.3 Community Adoption

854 We have provided a free distribution of the OSSP algorithm and the training sets discussed in section 3.4 and 4 as a
855 companion to this publication, complete with detailed startup guides and documentation. This OSSP algorithm has
856 been implemented entirely in Python using open source resources with release to additional users in mind. The code,
857 along with documentation, instructional guidelines, and premade training sets (those used for the analyses herein) is
858 available at <https://github.com/wrightni>. The software is packaged with default parameters and version controlled
859 training sets for 4 different imagery sources. The package includes a graphical user interface to allow users to build
860 custom training datasets that suit their individual needs. The algorithm was constructed with the flexibility to allow
861 for the classification of any number of features given an appropriate training dataset.

862 Our intention is that by providing easy access to the code in an open source format, we will enable both specific
863 inquiries and larger scale image processing that supports community efforts at general sea ice monitoring. We plan to
864 continue improving and updating the code as it gains users and we receive community feedback. We hope to encourage
865 others to design their own features and add-ons. Since the predictive ability of the machine learning algorithm
866 improves as more training data is added, we wish to strongly encourage the use of the GUI to produce additional
867 training sets and we plan to collate other users training sets into improved training versions. See documentation of the
868 training set creation GUI for more information on how to share a training set.

869 The OSSP algorithm helps to bring the goal of having a standardized method for deriving geophysical parameters
870 from high resolution optical sea ice imagery closer to reality. In the larger picture, developing such a tool is only the
871 first step. We recall that the motivation behind this development was the need to quantify sea ice surface conditions
872 in a way that could enable better understanding of the processes driving changes in sea ice cover. The value of the
873 toolkit will only be realized if it is used for these scientific inquiries. We look forward to working with imagery owners
874 to facilitate processing of additional datasets.

875 6. Conclusions

876 We have implemented a method for classifying the sea ice surface conditions from high resolution optical imagery of
877 sea ice. We designed the system to have a low barrier to entry, by coding it in an open source format, providing
878 detailed documentation, and releasing it publicly for community use. The code identifies the dominant surface types
879 found in sea ice imagery; open water, melt ponds, [and submerged ice, and snow](#) and ice, with accuracy that averages
880 96 percent – comparable to the consistency between manual expert human classifications of the imagery. The
881 algorithm is shown to be capable of classifying imagery from a range of image sensing platforms including
882 panchromatic and pansharpened WorldView satellite imagery, aerial sRGB imagery, and optical DMS imagery from

Deleted: ,

884 NASA IceBridge missions. Furthermore, the software can process imagery collected across the seasonal evolution of
885 the sea ice from early spring through complete ice melt, demonstrating it is robust even as the characteristics of the
886 ice features seasonally evolve. We conclude, based on our error analysis, that this automatic image processing method
887 can be used with confidence in analyzing the melt pond evolution at remote sites.

888 With appropriate processing, high resolution imagery collections should be a powerful tool for standardized and
889 routine observation of sea ice surface characteristics. We hope that providing easy access to the methods and algorithm
890 developed herein, we will facilitate the sea ice community convergence on a standardized method for processing high
891 resolution optical imagery either by adoption of this method, or by suggestion of an alternate method complete with
892 code release and error analysis.

893

894 The authors declare that they have no conflict of interest.

895

896 *Data Availability.* The OSSP algorithm code is available from <https://github.com/wrightni> during the review process,
897 and will be transferred to a permanent repository for publication. Image data and processing results are available at
898 the NSF Arctic Data Center (ADC). Raw and preprocessed image data from DigitalGlobe WorldView images will not
899 be made available for copyright reasons, but can be acquired from DigitalGlobe or the Polar Geospatial Center at the
900 University of Minnesota.

901

902 *Acknowledgements.* This work was supported by the Office of Naval Research Award N0001413MP20144 and the
903 National Science Foundation Award PLR-1417436. We would like to thank Donald Perovich and Alexandra Arntsen
904 for their assistance in creating machine learning training datasets. We would also like to thank Arnold Song, Justin
905 Chen, and Elias Deeb for their assistance and guidance with the development of the OSSP code. WorldView satellite
906 imagery was provided with the DigitalGlobe NextView License through the University of Minnesota Polar Geospatial
907 Center. A collection of the aerial imagery was collected by the SIZONet project. Some data used in this paper were
908 acquired by [the NASA](#) Operation IceBridge Project.

Deleted:), and a permanent DOI is pending.

909 References

910 [Arntsen, A. E., Song, A. J., Perovich, D. K. and Richter-Menge, J. A.: Observations of the summer
911 breakup of an Arctic sea ice cover, *Geophys. Res. Lett.*, 42\(19\), 8057–8063,
912 \[doi:10.1002/2015GL065224, 2015.\]\(#\)](#)

913 Blaschke, T.: Object based image analysis for remote sensing, *ISPRS J. Photogramm. Remote
914 Sens.*, 65(1), 2–16, [doi:10.1016/j.isprsjprs.2009.06.004](#), 2010.

915 Blaschke, T., Hay, G. J., Kelly, M., Lang, S., Hofmann, P., Addink, E., Queiroz Feitosa, R., van der
916 Meer, F., van der Werff, H., van Coillie, F. and Tiede, D.: Geographic Object-Based Image Analysis
917 – Towards a new paradigm, *ISPRS J. Photogramm. Remote Sens.*, 87, 180–191,
918 [doi:10.1016/j.isprsjprs.2013.09.014](#), 2014.

919 Breiman, L.: Bagging Predictors, *Mach. Learn.*, 24(2), 123–140, [doi:10.1023/A:1018054314350](#),
920 1996.

Deleted: NASA's

923 Breiman, L.: Random Forests, *Mach. Learn.*, 45(1), 5–32, doi:10.1023/A:1010933404324, 2001.
924 Curry, J. A., Schramm, J. L. and Ebert, E. E.: Sea ice-albedo climate feedback mechanism, *J. Clim.*,
925 8(2), 240–247, doi:10.1175/1520-0442(1995)008<0240:SIACFM>2.0.CO;2, 1995.
926 DeFries, R. .: Multiple Criteria for Evaluating Machine Learning Algorithms for Land Cover
927 Classification from Satellite Data, *Remote Sens. Environ.*, 74(3), 503–515, doi:10.1016/S0034-
928 4257(00)00142-5, 2000.
929 DeMott, P. J. and Hill, T. C. J.: Investigations of Spatial and Temporal Variability of Ocean and Ice
930 Conditions in and Near the Marginal Ice Zone. The “Marginal Ice Zone Observations and
931 Processes Experiment” (MIZOPEX) Final Campaign Summary, DOE ARM Climate Research Facility,
932 Pacific Northwest National Laboratory; Richland, Washington., 2016.
933 Dominguez, R.: IceBridge DMS L0 Raw Imagery, Version 1, , doi:10.5067/UMFN22VHGGMH,
934 2010.
935 Duro, D. C., Franklin, S. E. and Dubé, M. G.: A comparison of pixel-based and object-based image
936 analysis with selected machine learning algorithms for the classification of agricultural
937 landscapes using SPOT-5 HRG imagery, *Remote Sens. Environ.*, 118, 259–272,
938 doi:10.1016/j.rse.2011.11.020, 2012.
939 Eicken, H.: Tracer studies of pathways and rates of meltwater transport through Arctic summer
940 sea ice, *J. Geophys. Res.*, 107(C10), 8046, doi:10.1029/2000JC000583, 2002.
941 [Fetterer, F. and Untersteiner, N.: Observations of melt ponds on Arctic sea ice, *J. Geophys. Res.*](#)
942 [Ocean., 103\(C11\), 24821–24835, doi:10.1029/98JC02034, 1998.](#)
943 GDAL: GDAL - Geospatial Data Abstraction Library, Version 2.1.0, Open Source Geospatial Found.
944 [online] Available from: <http://gdal.org>, 2016.
945 Inoue, J., Curry, J. A. and Maslanik, J. A.: Application of Aerosondes to Melt-Pond Observations
946 over Arctic Sea Ice, *J. Atmos. Ocean. Technol.*, 25(2), 327–334, doi:10.1175/2007JTECHA955.1,
947 2008.
948 Kurtz, N. T., Farrell, S. L., Studinger, M., Galin, N., Harbeck, J. P., Lindsay, R., Onana, V. D., Panzer,
949 B. and Sonntag, J. G.: Sea ice thickness, freeboard, and snow depth products from Operation
950 IceBridge airborne data, *Cryosph.*, 7(4), 1035–1056, doi:10.5194/tc-7-1035-2013, 2013.
951 Kwok, R.: Declassified high-resolution visible imagery for Arctic sea ice investigations: An
952 overview, *Remote Sens. Environ.*, 142, 44–56, doi:10.1016/j.rse.2013.11.015, 2014.
953 Kwok, R. and Rothrock, D. A.: Decline in Arctic sea ice thickness from submarine and ICESat
954 records: 1958–2008, *Geophys. Res. Lett.*, 36(15), n/a-n/a, doi:10.1029/2009GL039035, 2009.
955 Landy, J., Ehn, J., Shields, M. and Barber, D.: Surface and melt pond evolution on landfast first-
956 year sea ice in the Canadian Arctic Archipelago, *J. Geophys. Res. Ocean.*, 119(5), 3054–3075,
957 doi:10.1002/2013JC009617, 2014.
958 Laxon, S. W., Giles, K. A., Ridout, A. L., Wingham, D. J., Willatt, R., Cullen, R., Kwok, R., Schweiger,
959 A., Zhang, J., Haas, C., Hendricks, S., Krishfield, R., Kurtz, N., Farrell, S. and Davidson, M.: CryoSat-
960 2 estimates of Arctic sea ice thickness and volume, *Geophys. Res. Lett.*, 40(4), 732–737,
961 doi:10.1002/grl.50193, 2013.
962 Lu, P., Li, Z., Cheng, B., Lei, R. and Zhang, R.: Sea ice surface features in Arctic summer 2008: Aerial
963 observations, *Remote Sens. Environ.*, 114(4), 693–699, doi:10.1016/j.rse.2009.11.009, 2010.
964 Markus, T., Cavalieri, D. J., Tschudi, M. A. and Ivanoff, A.: Comparison of aerial video and Landsat
965 7 data over ponded sea ice, *Remote Sens. Environ.*, 86(4), 458–469, doi:10.1016/S0034-

966 4257(03)00124-X, 2003.

967 Markus, T., Stroeve, J. C. and Miller, J.: Recent changes in Arctic sea ice melt onset, freezeup, and

968 melt season length, *J. Geophys. Res.*, 114(C12), C12024, doi:10.1029/2009JC005436, 2009.

969 Maslanik, J., Stroeve, J., Fowler, C. and Emery, W.: Distribution and trends in Arctic sea ice age

970 through spring 2011, *Geophys. Res. Lett.*, 38(13), doi:10.1029/2011GL047735, 2011.

971 Miao, X., Xie, H., Ackley, S. F., Perovich, D. K. and Ke, C.: Object-based detection of Arctic sea ice

972 and melt ponds using high spatial resolution aerial photographs, *Cold Reg. Sci. Technol.*, 119,

973 211–222, doi:10.1016/j.coldregions.2015.06.014, 2015.

974 [Miao, X., Xie, H., Ackley, S. F. and Zheng, S.: Object-Based Arctic Sea Ice Ridge Detection From](#)

975 [High-Spatial-Resolution Imagery, *IEEE Geosci. Remote Sens. Lett.*, 13\(6\), 787–791,](#)

976 [doi:10.1109/LGRS.2016.2544861, 2016.](#)

977 Pal, M.: Random forest classifier for remote sensing classification, *Int. J. Remote Sens.*, 26(1),

978 217–222, doi:10.1080/01431160412331269698, 2005.

979 Parkinson, C. L. and Comiso, J. C.: On the 2012 record low Arctic sea ice cover: Combined impact

980 of preconditioning and an August storm, *Geophys. Res. Lett.*, 40(7), 1356–1361,

981 doi:10.1002/grl.50349, 2013.

982 Pedregosa, F., Varoquaux, G., Gramfort, A., Michel, V., Thirion, B., Grisel, O., Blondel, M.,

983 Prettenhofer, P., Weiss, R., Dubourg, V., Vanderplas, J., Passos, A., Cournapeau, D., Brucher, M.,

984 Perrot, M. and Duchesnay, É.: Scikit-learn: Machine Learning in Python, *J. Mach. Learn. Res.*,

985 12(Oct), 2825–2830 [online] Available from:

986 <http://jmlr.csail.mit.edu/papers/v12/pedregosa11a.html> (Accessed 24 July 2017), 2011.

987 Perovich, D. K.: On the aggregate-scale partitioning of solar radiation in Arctic sea ice during the

988 Surface Heat Budget of the Arctic Ocean (SHEBA) field experiment, *J. Geophys. Res.*, 110(C3),

989 C03002, doi:10.1029/2004JC002512, 2005.

990 Perovich, D. K., Tucker, W. B. and Ligett, K. A.: Aerial observations of the evolution of ice surface

991 conditions during summer, *J. Geophys. Res.*, 107(C10), 8048, doi:10.1029/2000JC000449, 2002a.

992 Perovich, D. K., Grenfell, T. C., Light, B. and Hobbs, P. V.: Seasonal evolution of the albedo of

993 multiyear Arctic sea ice, *J. Geophys. Res.*, 107(C10), 8044, doi:10.1029/2000JC000438, 2002b.

994 Perovich, D. K., Richter-Menge, J. A., Jones, K. F. and Light, B.: Sunlight, water, and ice: Extreme

995 Arctic sea ice melt during the summer of 2007, *Geophys. Res. Lett.*, 35(11), L11501,

996 doi:10.1029/2008GL034007, 2008.

997 Petty, A. A., Tsamados, M. C., Kurtz, N. T., Farrell, S. L., Newman, T., Harbeck, J. P., Feltham, D. L.

998 and Richter-Menge, J. A.: Characterizing Arctic sea ice topography using high-resolution IceBridge

999 data, *Cryosph.*, 10(3), 1161–1179, doi:10.5194/tc-10-1161-2016, 2016.

1000 Pistone, K., Eisenman, I. and Ramanathan, V.: Observational determination of albedo decrease

1001 caused by vanishing Arctic sea ice, *Proc. Natl. Acad. Sci.*, 111(9), 3322–3326,

1002 doi:10.1073/pnas.1318201111, 2014.

1003 Polashenski, C., Perovich, D. and Courville, Z.: The mechanisms of sea ice melt pond formation

1004 and evolution, *J. Geophys. Res. Ocean.*, 117(C1), n/a-n/a, doi:10.1029/2011JC007231, 2012.

1005 Renner, A. H. H., Gerland, S., Haas, C., Spreen, G., Beckers, J. F., Hansen, E., Nicolaus, M. and

1006 Goodwin, H.: Evidence of Arctic sea ice thinning from direct observations, *Geophys. Res. Lett.*,

1007 41(14), 5029–5036, doi:10.1002/2014GL060369, 2014.

1008 Rösel, A. and Kaleschke, L.: Comparison of different retrieval techniques for melt ponds on Arctic

1009 sea ice from Landsat and MODIS satellite data, *Ann. Glaciol.*, 52(57), 185–191,
1010 doi:10.3189/172756411795931606, 2011.

1011 Rösel, A., Kaleschke, L. and Birnbaum, G.: Melt ponds on Arctic sea ice determined from MODIS
1012 satellite data using an artificial neural network, *Cryosph.*, 6(2), 431–446, doi:10.5194/tc-6-431-
1013 2012, 2012.

1014 Stroeve, J. C., Serreze, M. C., Holland, M. M., Kay, J. E., Malanik, J. and Barrett, A. P.: The Arctic's
1015 rapidly shrinking sea ice cover: a research synthesis, *Clim. Change*, 110, 1005–1027,
1016 doi:10.1007/s10584-011-0101-1, 2012.

1017 Stroeve, J. C., Markus, T., Boisvert, L., Miller, J. and Barrett, A.: Changes in Arctic melt season and
1018 implications for sea ice loss, *Geophys. Res. Lett.*, 41, 1216–1225,
1019 doi:10.1002/2013GL058951. Received, 2014.

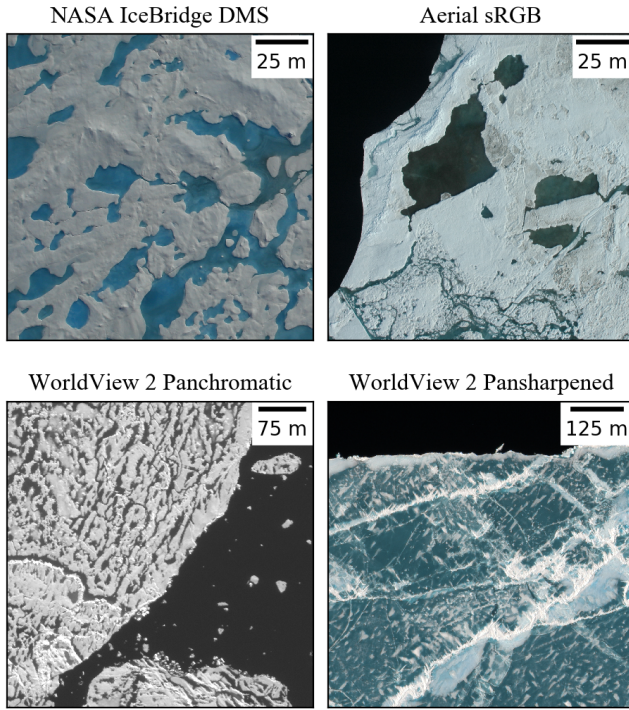
1020 Tschudi, M. A., Maslanik, J. A. and Perovich, D. K.: Derivation of melt pond coverage on Arctic sea
1021 ice using MODIS observations, *Remote Sens. Environ.*, 112(5), 2605–2614,
1022 doi:10.1016/j.rse.2007.12.009, 2008.

1023 van der Walt, S., Schönberger, J. L., Nunez-Iglesias, J., Boulogne, F., Warner, J. D., Yager, N.,
1024 Gouillart, E. and Yu, T.: scikit-image: image processing in Python, *PeerJ*, 2, e453,
1025 doi:10.7717/peerj.453, 2014.

1026 Webster, M. A., Rigor, I. G., Perovich, D. K., Richter-menge, J. A., Polashenski, C. M. and Light, B.:
1027 Seasonal evolution of melt ponds on Arctic sea ice, *J. Geophys. Res. Ocean.*, 120(9), 1–15,
1028 doi:10.1002/2015JC011030. Received, 2015.

1029 Yan, G., Mas, J. -F., Maathuis, B. H. P., Xiangmin, Z. and Van Dijk, P. M.: Comparison of pixel-based
1030 and object-oriented image classification approaches—a case study in a coal fire area, Wuda,
1031 Inner Mongolia, China, *Int. J. Remote Sens.*, 27(18), 4039–4055,
1032 doi:10.1080/01431160600702632, 2006.

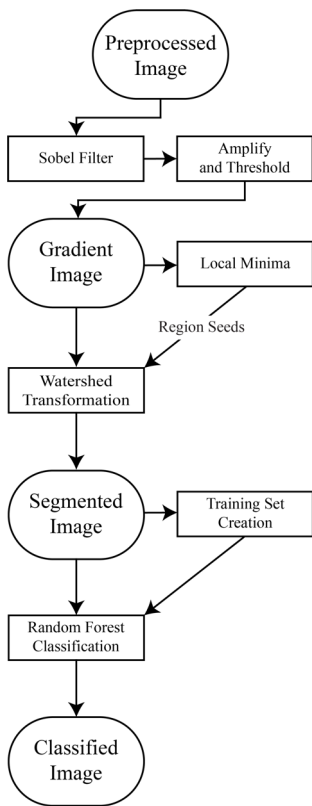
1033 Figures



1034
1035
1036

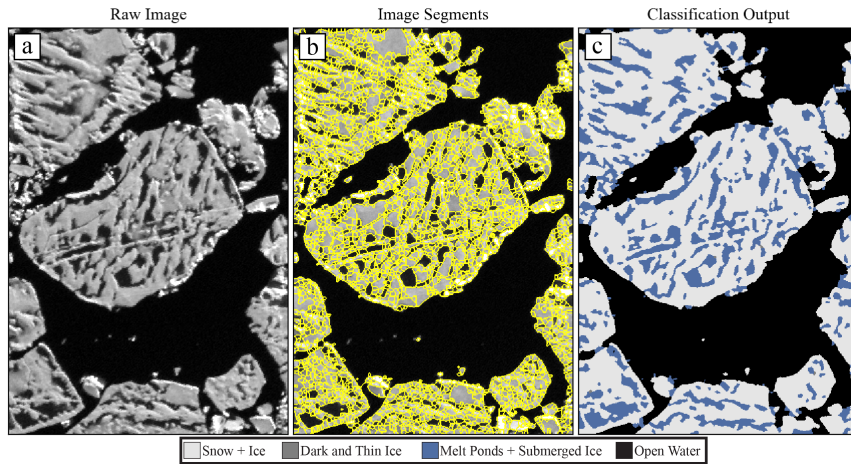
Figure 1. Examples of imagery from each of the four imaging platforms that we seek to classify in this study. Each type of imagery has either a different spatial resolution or and different levels spectral information available.

- Deleted: types
- Deleted: process
- Deleted: Note the varying
- Deleted: sources, resolutions,
- Deleted: for each image type



1042
 1043
 1044
 1045

Figure 2. Flow diagram depicting the steps taken to classify an image in the OSSP algorithm.



046

047

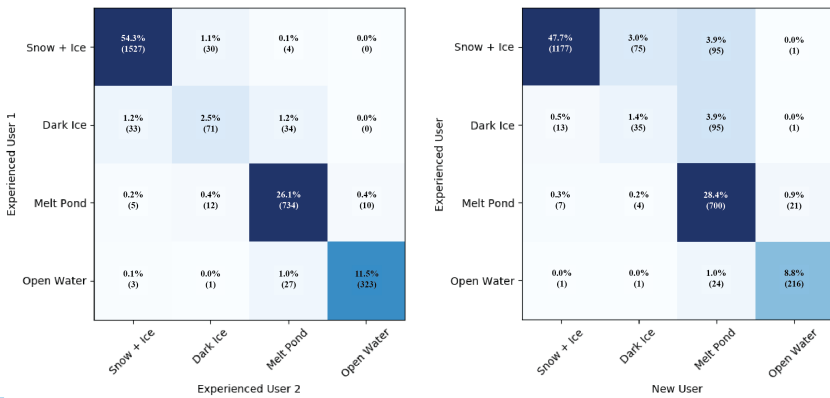
048

049

050

051

Figure 3. Visual representation of important steps in the image processing workflow. Panel (a) shows preprocessed panchromatic WorldView 2 satellite imagery, taken on July 1, 2014. In panel (b), outlines of the image objects created by our edge detection and watershed transformation are shown overlain on top of the image in panel (a). Panel (c) shows the result of replacing each object with a value corresponding to the prediction of the random forest classifier.



052

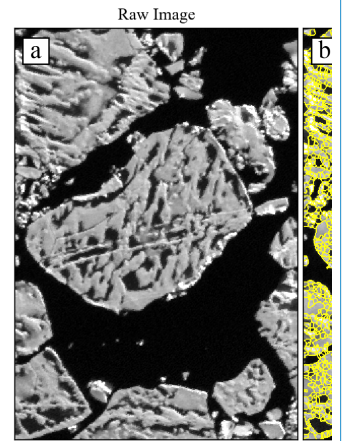
053

054

055

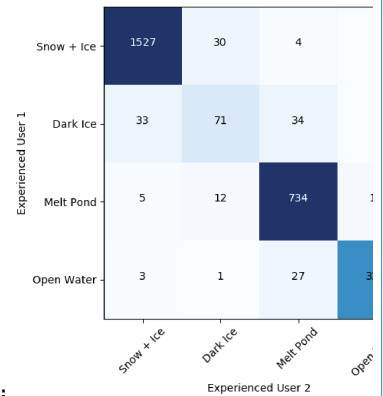
056

Figure 4. Confusion matrices comparing classification tendencies between two users experienced with the image processing algorithm (left) and between an experienced user and a new user (right). Squares are colored based on the value of the cell, with darker colors indicating more matches. Values along the diagonal of each confusion matrix represents the agreement between each user, while values in off-diagonal regions represent disagreement.



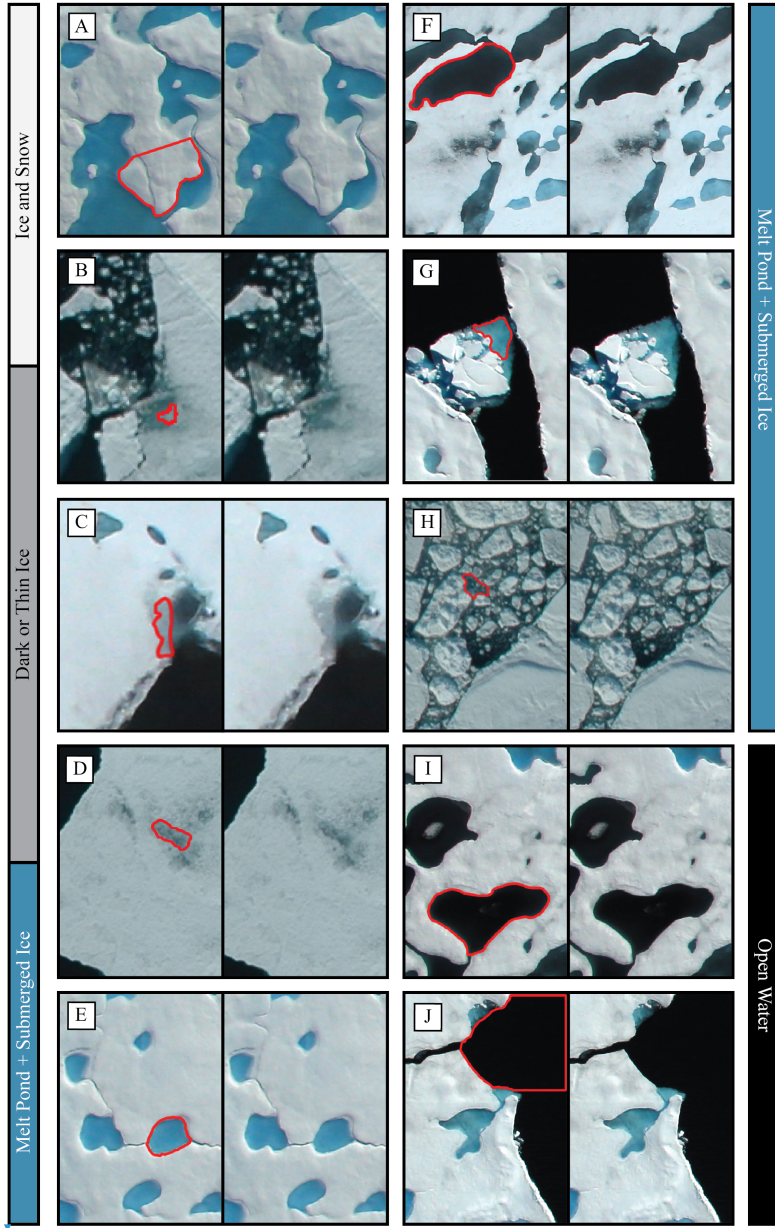
Deleted:

Deleted: Important...visual representation of important steps in the image processing workflow. Panel (a) shows a section of a preprocessed panchromatic WorldView 2 satellite image...magery, taken on July 1, 2014. Panel...n panel (b) shows), outlines of the outline of ...image objects created from...y our edge detection and watershed transformation...are shown overlain on top of the image in panel (a). Panel (c) shows the classified ...result after running...f replacing each object through a

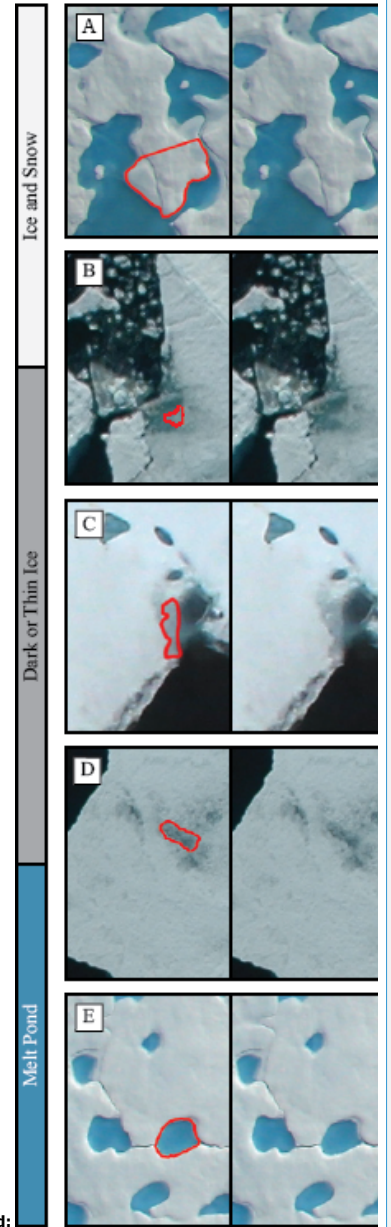


Deleted:

Deleted: patterns...endencies between two users experienced with the image processing algorithm (left) and between an experienced user and a new user (right). Squares are colored based on the number...alue of pixels in that...he cell, with darker colors indicating a larger number...ore matches. Values along the diagonal of pixels.

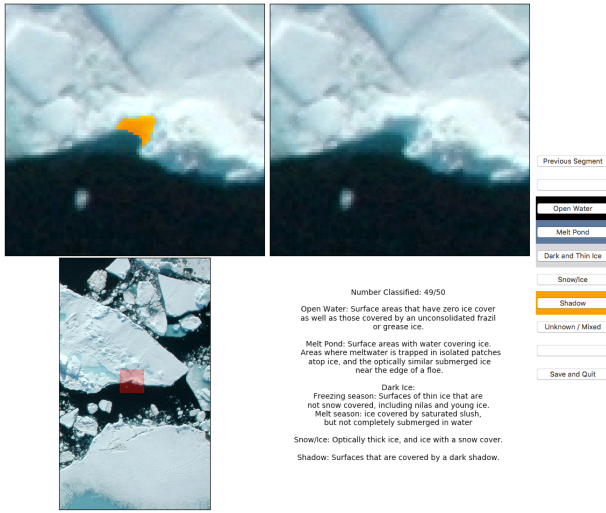


Deleted:



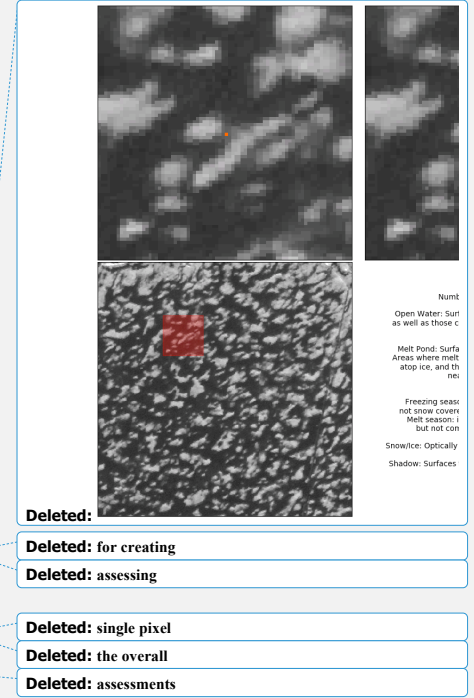
1095
1096
1097
1098
1099
1100

Figure 5. Examples of surfaces seen in aerial imagery of sea ice that span our four classification categories. Panel A: snow covered surface. Panel B: Ice with a thin surface scattering layer where disagreement on true classification exists - represents a small fraction of total surface area. Panel C: Panel D: Surface transitioning to a melt pond that is not yet fully submerged. Panel E: Melt pond. Panel F: Dark melt pond that has not completely melted through. Panel G: Submerged ice. Panel H: Brush, mostly submerged, included in the melt pond category. Panel I: Melt pond that has completely melted through to open water. Panel J: Open water.



101
102
103
104
105
106
107
108

Figure 6. Graphical user interface used to create training datasets and to assess the accuracy of a classified image. Bottom left panel shows an overview of the region to provide the user with spatial context. Top left magnifies the image and highlights the segment of interest, while top right shows the same region with no segment overlap. The user is allowed to choose between any of the relevant surface categories, or to indicate that they are unsure of the classification. As shown, the user interface is demonstrating the classification of a segment for use in a training set. This same GUI is also capable of asking a user to classify an individual pixel, which can be compared to the final classified image for determining accuracy (section 3.6).



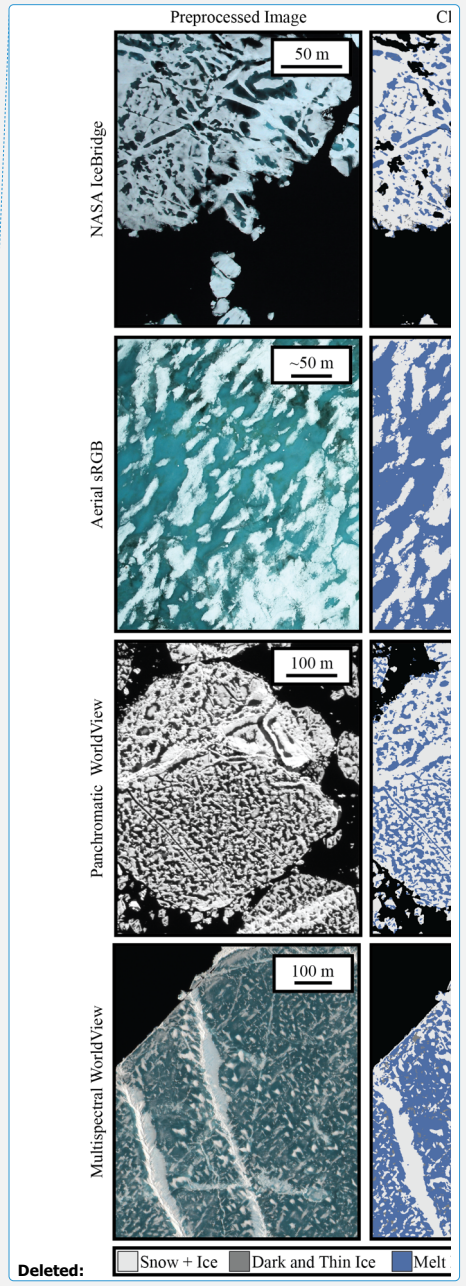
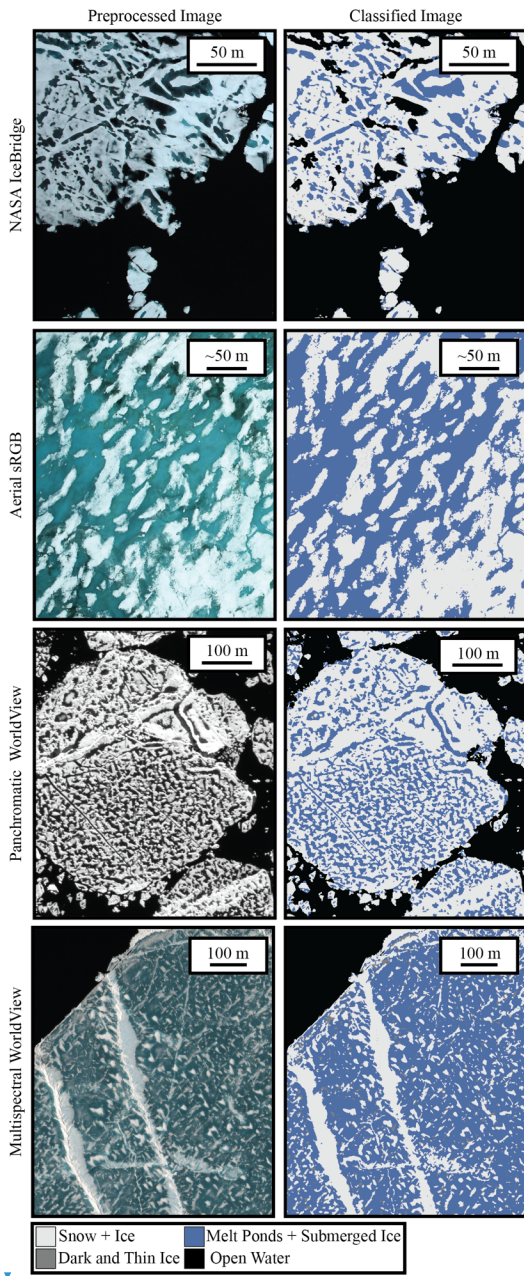
Deleted: for creating

Deleted: assessing

Deleted: single pixel

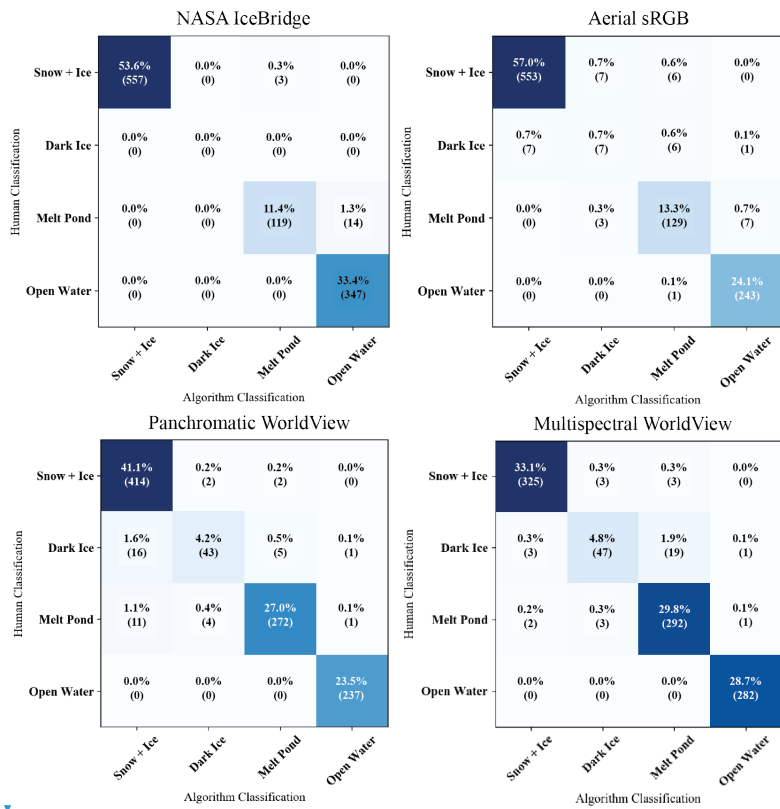
Deleted: the overall

Deleted: assessments



118
119
120

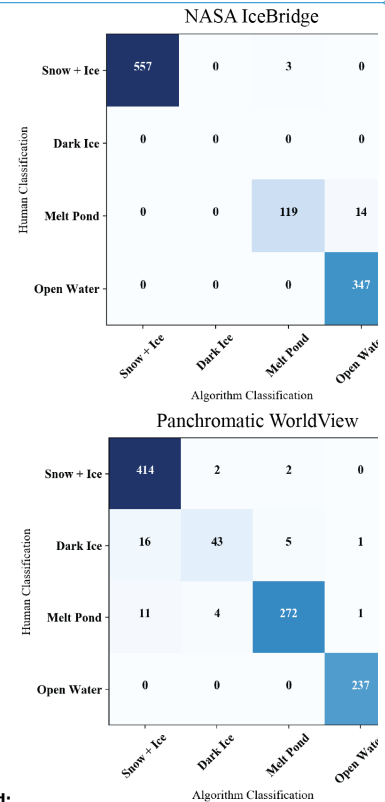
Figure 7. Side-by-side comparison of preprocessed imagery (left) and the result of classification (right) for each of the four imaging platforms. Images depict ice surfaces in varying stages of melt. The NASA IceBridge image, for example, is in very late stages of melt ponds that have already melted through to the ocean.



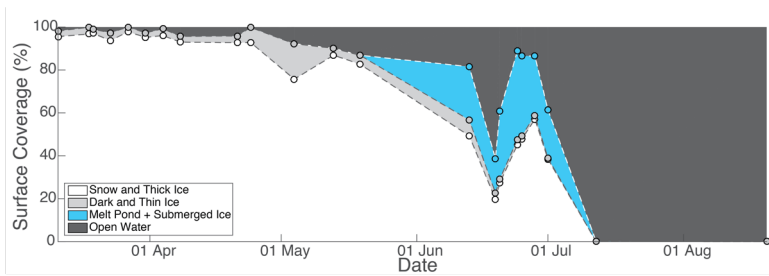
121
122
123
124
125

Figure 8. Accuracy confusion matrices comparing the classification of 1000-pixels between a human and the algorithm. Squares are colored based on the value of the cell, with darker colors indicating more matches. Values along the diagonal of each confusion matrix represents the agreement between each classifier, while values in off-diagonal regions represent disagreement.

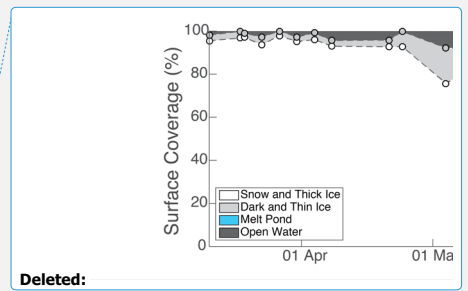
Deleted: classified
Deleted: . One scene was selected from each imagery source.
Deleted: imagery
Deleted: with many
Deleted: having



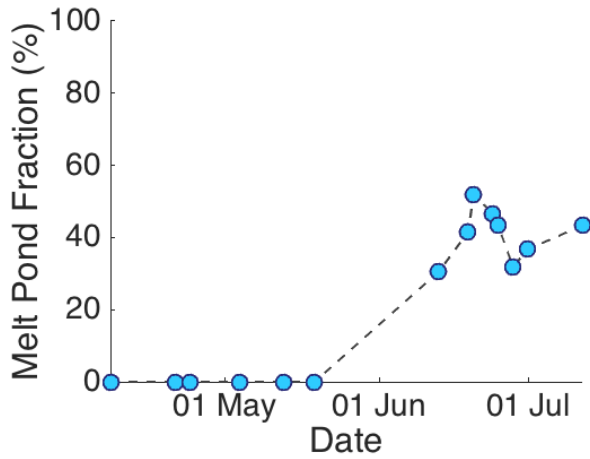
Deleted:
Deleted: 1000-pixel accuracy
Deleted: matrix for each image type.
Deleted: number
Deleted: pixels in that
Deleted: a larger number of pixels



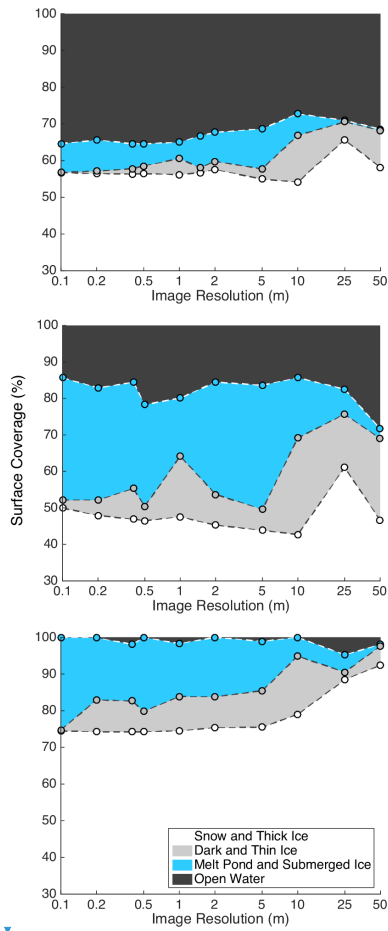
137
138 **Figure 9. Seasonal progression of surface type distributions at the satellite image collection site; 2014 in the Beaufort Sea**
139 **at 72°N 128°W. This site represents a Eulerian observation of the sea ice surface, and does not track a floe across its lifetime.**
140 **Average scene size was 956km² with a minimum of 304km² and a maximum of 1321km².**



Deleted:
Deleted: our



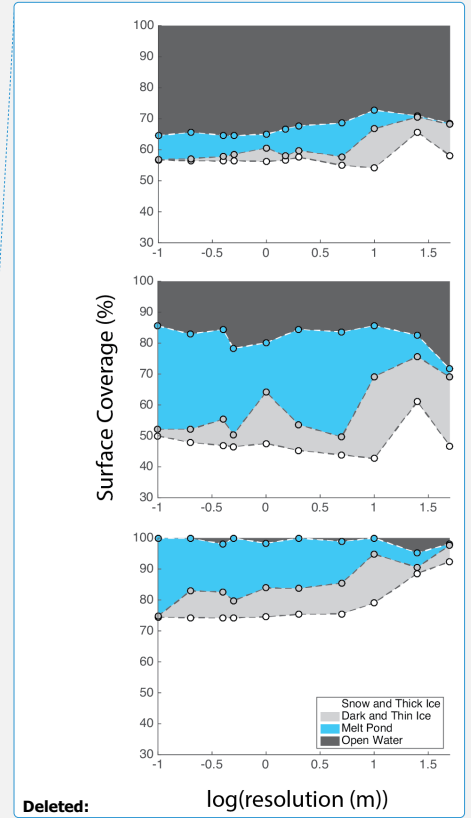
1142
1143 **Figure 10. Evolution of melt pond fraction over the 2014 season at our satellite image collection site; 2014 in the Beaufort**
1144 **Sea at 72°N 128°W. This site represents a Eulerian observation of the sea ice surface, and does not track a floe across its**
1145 **lifetime. By August, the sea ice extent has retreated north of this location, and we therefore do not capture a full melt pond**
1146 **cycle.**



150

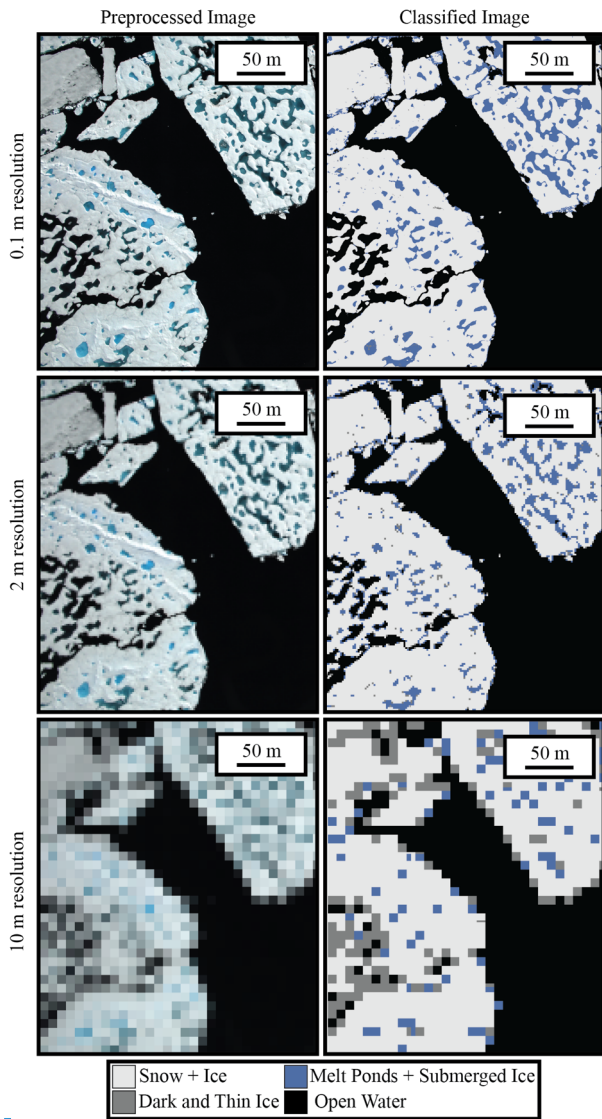
151
152
153

Figure 11. Change in surface coverage percentage as a result of downsampling [three IceBridge images](#). Each plot represents a single image, with resolution along the x-axis on a log scale. Imagery starts at the nominal IceBridge resolution of 0.1m and is degraded to a maximum of 50m.



Deleted:

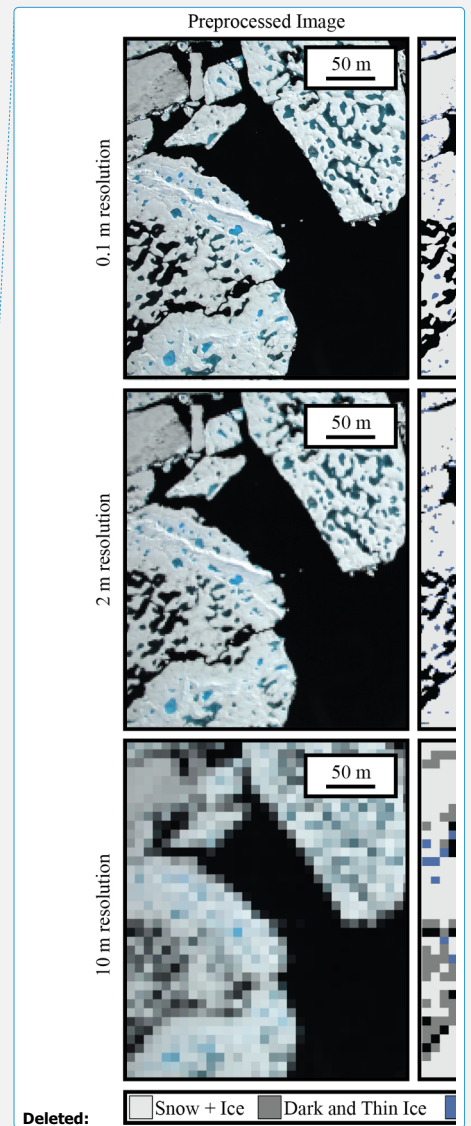
Deleted: imagery.



156
157
158
159
160

Figure 12. Visual demonstration of the downsampling effect on a single NASA IceBridge image. The top image is shown at the original 0.1 m resolution. The middle image is a resolution of 2m - the equivalent of a multispectral WorldView 2 image without pansharping. The bottom has a resolution of 10m, where pixel size has begun to exceed the average melt pond size.

1161

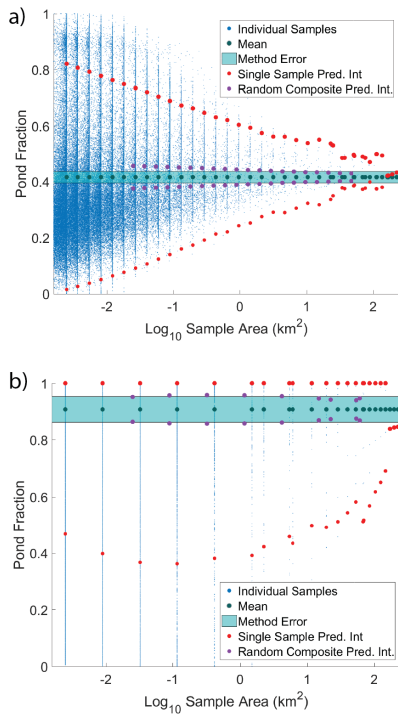


Deleted:

Deleted: resolution

Deleted: In the

Deleted: image



1166

1167

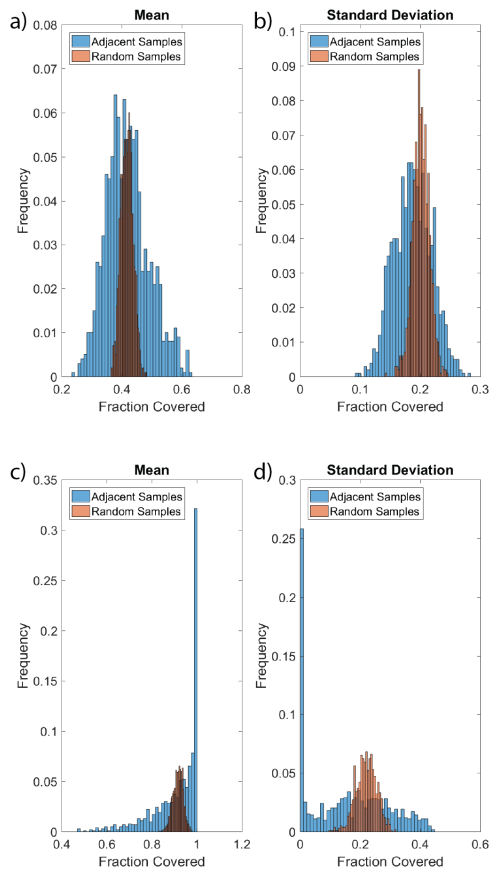
1168

1169

1170

1171

Figure 13. Convergence of melt pond fraction (a) and ice fraction (b) for a WorldView image collected 25 June 2014 at 72°N 128°W as the area evaluated is increased. Small blue dots represent individual image subsets. For segments of a given size, black dots represent the mean value of those samples, red dots represent the 95% prediction interval, and purple dots show the 95% prediction interval for the same total area, but calculated from 100 randomly placed, smaller, samples. Cyan shaded area represents the error in determination expected from the processing method.



1172

1173

1174

1175

1176

Figure 14. Histogram of mean (a) and standard deviation (b) of 1000 melt pond fraction estimates, each calculated from 100 sample areas on a 25 June 2014 WorldView image. The 100 samples were either randomly distributed across the image (red) or adjacent to each other (blue). Panels (c) and (d) show the same as (a) and (b), respectively, for ice fraction rather than melt pond fraction.

1177

1178

1179

1180

1181

1182

Attribute	MS	PAN	Aerial
Mean (Pan)			
Mean (Coastal)			
Mean (Blue)			
Mean (Green)			
Mean (Yellow)			
Mean (Red)			
Mean (Red Edge)			
Mean (NIR1)			
Mean (NIR2)			
Median (Pan)			
StDev (Pan)			
Min Intensity (Pan)			
Max Intensity (Pan)			
StDev (Blue)			
StDev (Green)			
StDev (Red)			
Entropy			
Segment Size			
Image Date			
Coastal / Green			
Blue / NIR1			
Green / NIR1			
Yellow / Red Edge			
Yellow / NIR1			
Yellow / NIR2			
Red / NIR1			
(B1 - NIR1)/(B2 + NIR1)			
(G - R)/(G + R)			
(B - R)/(B + R) ¹			
(B - G)/(B + G) ¹			
(G - R)/(2*B - G - R) ¹			
Neighbor Mean			
Neighbor StDev			
Neighbor Max			
Neighbor Entropy			

1184 Miao et al. 2015

1185 Table 1. Attributes used for classifying each of the three image types. Blue squares indicate attributes that were used for
 1186 that image. Dark gray squares indicate attributes that are available, but were not found to be sufficiently beneficial in the
 1187 classification to merit inclusion under our criteria. Light gray squares indicate attributes that are not available on that image
 1188 type (e.g. band ratios on a panchromatic image). NIR is the near infrared wavelength. B1 is the coastal WorldView band,
 1189 and B2 is the blue band. R, G, and B, stand for red, green, and blue, respectively.

- Deleted: , dark
- Deleted: are ones where the
- Deleted: is
- Deleted: are
- Deleted: wavelengths
- Deleted: B
- Deleted: G

Image ID	Sensor Type	Date Collected	Ice + Snow	DTI	MPS	OW	Accuracy
102001002C214D00	Panchromatic	11-Mar-14	96	3	0	2	97
103001002E8F0D00	Panchromatic	18-Mar-14	97	3	0	0	97
102001002BBA0C00	Panchromatic	19-Mar-14	97	2	0	1	96
103001002FC75200	Panchromatic	23-Mar-14	94	4	0	3	95
102001002CB77C00	Panchromatic	27-Mar-14	98	2	0	0	100
1030010030403A00	Panchromatic	31-Mar-14	95	2	0	3	98
1030010031B65000	Panchromatic	4-Apr-14	96	3	0	1	99
102001002BA6C100	Panchromatic	8-Apr-14	93	3	0	4	100
103001002F79A700	Panchromatic	21-Apr-14	93	3	0	4	98
1030010030371B00	Panchromatic	24-Apr-14	93	7	0	0	98
103001003102A600	Panchromatic	4-May-14	76	16	0	8	98
102001003007FA00	Panchromatic	13-May-14	87	3	0	10	97
10300100306F2E00	Panchromatic	19-May-14	83	4	0	13	96
102001003035D700	Panchromatic	13-Jun-14	49	7	25	18	95
1030010033AAC400	Panchromatic	19-Jun-14	20	3	16	61	97
1020010031DF9E00	Panchromatic	20-Jun-14	27	2	31	39	96
1020010032B94E00	Panchromatic	24-Jun-14	45	2	41	11	95
102001003122A700	Panchromatic	25-Jun-14	48	1	37	13	97
102001002F4F1A00	Panchromatic	28-Jun-14	57	2	28	14	95
10300100346D1200	Panchromatic	1-Jul-14	38	0	23	39	97
1030010035C8D000	Panchromatic	12-Jul-14	0	0	0	100	100
103001003421AB00	Panchromatic	20-Aug-14	0	0	0	100	100

Deleted: I+S

Deleted: MP

10300100324B7D00	Multispectral	13-Jun-14	44	7	29	19	96
1030010033AAC400	Multispectral	19-Jun-14	16	3	19	62	97
10300100346D1200	Multispectral	1-Jul-14	44	2	26	28	98
1030010035C8D000	Multispectral	12-Jul-14	0	0	0	100	100
2016_07_13_05863	IceBridge	13-Jul-16	50	2	34	14	92
2016_07_13_05882	IceBridge	13-Jul-16	72	1	26	0	97
2016_07_13_05996	IceBridge	13-Jul-16	70	2	28	0	95
2016_07_13_06018	IceBridge	13-Jul-16	61	2	36	1	91
2016_07_13_06087	IceBridge	13-Jul-16	66	1	33	0	99
2016_07_16_00373	IceBridge	16-Jul-16	9	0	2	89	100
2016_07_16_00385	IceBridge	16-Jul-16	66	1	14	20	98
2016_07_16_00662	IceBridge	16-Jul-16	49	1	16	35	98
2016_07_16_00739	IceBridge	16-Jul-16	67	2	25	6	97
2016_07_16_01569	IceBridge	16-Jul-16	22	0	7	71	97
2016_07_16_02654	IceBridge	16-Jul-16	35	0	10	54	95
2016_07_19_01172	IceBridge	19-Jul-16	62	0	14	24	90
2016_07_19_01179	IceBridge	19-Jul-16	57	0	10	32	95
2016_07_19_02599	IceBridge	19-Jul-16	51	0	7	43	99
2016_07_19_02603	IceBridge	19-Jul-16	69	0	9	22	99
2016_07_19_02735	IceBridge	19-Jul-16	74	0	25	0	100
2016_07_19_03299	IceBridge	19-Jul-16	57	0	8	35	96
2016_07_21_01221	IceBridge	21-Jul-16	49	0	4	47	97
2016_07_21_01311	IceBridge	21-Jul-16	87	1	5	7	95
2016_07_21_01316	IceBridge	21-Jul-16	92	0	4	4	99
DSC_0154	Aerial sRGB	8-Jun-09	43	4	53	0	94
DSC_0327	Aerial sRGB	8-Jun-09	33	3	63	0	90
DSC_0375	Aerial sRGB	8-Jun-09	96	0	4	0	99
DSC_0422	Aerial sRGB	8-Jun-09	88	0	11	0	98
DSC_0223	Aerial sRGB	10-Jun-09	46	1	53	0	93
DSC_0243	Aerial sRGB	10-Jun-09	59	1	40	1	98
DSC_0314	Aerial sRGB	10-Jun-09	89	0	11	0	95
DSC_0319	Aerial sRGB	10-Jun-09	75	2	19	4	88

DSC_0323	Aerial sRGB	10-Jun-09	37	2	61	0	95
DSC_0338	Aerial sRGB	10-Jun-09	83	2	15	1	95
DSC_0386	Aerial sRGB	10-Jun-09	80	3	14	3	89
DSC_0394	Aerial sRGB	10-Jun-09	79	2	10	9	95
DSC_0412	Aerial sRGB	10-Jun-09	63	2	24	10	92
DSC_0425	Aerial sRGB	10-Jun-09	56	2	17	24	97
DSC_0439	Aerial sRGB	10-Jun-09	71	1	6	22	98
DSC_0441	Aerial sRGB	10-Jun-09	57	0	4	38	98
DSC_0486	Aerial sRGB	10-Jun-09	53	1	17	29	96
DSC_0634	Aerial sRGB	10-Jun-09	72	1	14	12	96
DSC_0207	Aerial sRGB	13-Jun-09	80	1	19	0	96
DSC_0514	Aerial sRGB	13-Jun-09	86	1	13	0	97

1200 Results Table 2. The complete results of imagery processed for this analysis. Descriptions for each image includes the image
1201 type, date collected, the percent of the image that falls into each of the four categories, and the accuracy assessment.

1202

Image Source	Training Dataset Size	Out-of-bag Error
Panchromatic WorldView	1000	0.94
Pansharpened WorldView	859	0.89
Aerial Imagery	945	0.94
IceBridge Imagery	940	0.91

203 Table 3. Out-of-Bag scores for the three training datasets used to classify imagery from each of the four sensor platforms
204 and the number of objects manually classified for each set.

Deleted: .

Page 17: [1] Deleted **Nicholas C. Wright** **12/18/17 12:39:00 PM**

We next test the central limit theorem to see how well we can predict the error bounds from processing a single set of independent (i.e. randomly distributed) samples. The central limit theorem states that when taking the mean of a sufficiently large number of independent samples of a random variable, the standard error of the mean of the samples is equal to $\frac{\sigma}{\sqrt{N}}$ where σ is the standard deviation of the sample values and N is the sample size. The standard deviation of pond coverage fraction in sets of 100 sub-images ranged from 0.15 to 0.25 across the 1000 sample sets run (see histogram in Fig. 14b) This yields a predicted standard error of the mean determined from any one of these sets of 0.015 to 0.025. The observed standard deviation in the mean values across all 1000 sample sets presented in Fig. 14a is 0.0201, indicating that the central limit theorem applies in this case.

Returning

Page 17: [2] Deleted **Nicholas C. Wright** **12/18/17 12:39:00 PM**

, this time representing twice the standard error determined from the central limit theorem.

Page 17: [3] Deleted **Nicholas C. Wright** **12/18/17 12:39:00 PM**

permits expedient determination of melt pond fraction within that image area with small error bounds. If the total image is large enough, the value will be representative of the

Page 17: [4] Deleted **Nicholas C. Wright** **12/18/17 12:39:00 PM**

scale. In this case, processing as little as 5km² (~0.5%) of the image permits determination of a mean that lies within 0.025 of the true image mean 95% of the time. Also indicated on the plot is a 5% uncertainty band around the mean

Page 17: [5] Deleted **Nicholas C. Wright** **12/18/17 12:39:00 PM**

A test of the central value theorem again shows that it also applies in this case and provides a good estimate of the error of a mean ice fraction calculated from a set of random sub images. The green dots again indicate

Page 17: [6] Deleted **Nicholas C. Wright** **12/18/17 12:39:00 PM**

must process imagery representing at least 5km² in surface area, selected in at least

Page 25: [7] Deleted **Nicholas C. Wright** **12/18/17 12:39:00 PM**

Important

Page 25: [7] Deleted **Nicholas C. Wright** **12/18/17 12:39:00 PM**

Important

Page 25: [7] Deleted **Nicholas C. Wright** **12/18/17 12:39:00 PM**

Important

Page 25: [7] Deleted **Nicholas C. Wright** **12/18/17 12:39:00 PM**

Important

Page 25: [7] Deleted **Nicholas C. Wright** **12/18/17 12:39:00 PM**

Important

